

FILTERING OF ACOUSTIC INFORMATION FROM AERO-OPTICAL MEASUREMENTS

A Dissertation

Submitted to the Graduate School
of the University of Notre Dame
in Partial Fulfillment of the Requirements
for the Degree of

Doctor of Philosophy

by

Brian Lowell Catron

R. Mark Rennie , Co-Director

Eric J. Jumper, Co-Director

Graduate Program in Aerospace and Mechanical Engineering

Notre Dame, Indiana

September 2021

FILTERING OF ACOUSTIC INFORMATION FROM AERO-OPTICAL MEASUREMENTS

Abstract

by

Brian Lowell Catron

Abstract Goes Here

To my wife Karen & our son Arthur

CONTENTS

Figures	v
Tables	vii
Symbols	ix
Acknowledgments	xi
Chapter 1: Introduction	1
Chapter 2: Literature Review	5
2.1 Aero-Optics	5
2.1.1 A Brief History of Aero-Optics	8
2.2 Acoustics	9
2.2.1 Basic Acoustics	9
2.2.2 Duct Acoustics	10
2.2.2.1 Characteristic Equations of Cross-Sections	13
Chapter 3: Aero-Optical and Acoustical Coupling	17
3.1 Examples of Acoustic-Optical Coupling	17
3.1.1 Planar Acoustic Waves	17
3.1.2 Higher Order Duct Modes	20
3.1.3 Spherical Acoustic Waves	20
Chapter 4: Basic Wavefront Filtering Techniques	21
4.1 Dispersion Analysis	21
4.2 Dispersion Calculation	23
4.3 Synthetic Wavefront Generation	26
4.3.1 Aero-Optical Signal	27
4.3.2 Stationary Mode Signals	29
4.3.3 Sound & Vibration Signals	29
4.3.4 Mean Lensing Signal	29
4.3.5 Background Noise Signal	29
4.3.6 Synthetic Wavefront Creation	30
4.3.7 Comparison to Measured Data	33
4.4 Filtering Basics	33
4.5 Temporal Filter Methods	34
4.6 Upstream/Downstream Moving	37
4.7 Velocity Filtering	39
Appendix A: Sample Code	43
Bibliography	57

FIGURES

1.1	Diffraction-limited far-field intensity of a beam normalized by the performance at $1\mu\text{m}$.	2
1.2	Strehl ratio due to the OPD_{RMS} of the Airborne Laser Laboratory at various laser wavelengths. ALL had an estimated Strehl ratio of 95% with its $10.6\mu\text{m}$ laser. . . .	2
2.1	Gladstone-Dale constant for air over the visible wavelength range.	6
2.2	(a) Diffraction limited on target intensity as a function of wavelength normalized by the value at $\lambda = 1\mu\text{m}$. (b) Strehl ratio as a function of wavelength for an aberration that gives $\text{SR} = 0.95$ at $\lambda = 10.6\mu\text{m}$	8
2.3	OPD_{RMS} values necessary to obtain Strehl ratios of 0.9, 0.7, and 0.5 over a range of wavelengths.	9
2.4	Duct with a rectangular cross-section.	11
2.5	Characteristic solutions to Equation 2.26 with rigid wall in a rectangular cross-section where $m=0:2$ and $n=0:3$. Nodal lines are depicted by the dot-dash lines. The cross-sectional wave numbers, k_m , listed are for a duct of unit length and height.	14
2.6	Characteristic solutions to Equation 2.26 with rigid wall in a circular cross-section where $m=0:2$ and $n=0:3$. Nodal lines are depicted by the dot-dash lines. The cross-sectional wave numbers, k_m , listed are for a duct of unit radius.	15
3.1	General geometry for various sample calculations for showing the acoustic-optical coupling effect.	18
3.2	Theoretical time-averaged OPD_{RMS} per meter of beam propagation as a function of sound pressure level, SPL, for several Λ/Ap ratios and $\theta = 0$	18
3.3	Theoretical time-averaged OPD_{RMS} for a rms sound pressure of 1 Pa (SPL of 94 dB), l_n of 1 m, and various angles and Λ/Ap ratios.	19
3.4	Theoretical time-averaged OPD_{RMS} for the two acoustic waves (u+c and u-c) for the blade pass frequency (534 Hz) at Mach 0.6 with a RMS sound pressure of 1 Pa (SPL of 94 dB), l_n of 1 m, and Ap of 15 cm.	20
4.1	A simplified dispersion plot. Simulation of two broadband plane waves traveling in opposite directions through a 1-D wavefront.	22
4.2	Alternative representation of the simplified dispersion plot. Simulation of two broadband plane waves traveling in opposite directions through a 1-D wavefront.	23
4.3	Dispersion analysis isosurface at a value of $10^{-13}\mu\text{m}^2/\text{Hz}/\text{m}^{-2}$ from two different views. The isosurface encompasses 99.5% of the energy of the optical disturbances. .	24
4.4	Synthetic wavefront input dispersion plot of an aero-optical signal and various signal corruption components. The aero-optical signal is shown in red, the stationary modes in blue, duct acoustics in magenta, blade-passing frequency related corruption in green, slowly varying mean-lensing in yellow, and background in cyan.	28
4.5	Sample frames from the synthetic wavefront with the total wavefront signal on top and the aero-optical only signal bottom. Flow is from right to left.	31

4.6	Synthetic wavefront output dispersion plot of an aero-optical signal and various signal corruption components.	32
4.7	OPD time-averaged spatial-RMS of high-pass temporal filters relative to the aero-optical only unfiltered wavefront.	34
4.8	Measured wavefronts filtered at the blade-passing frequency (532 ± 10 Hz). The left column is band-stop filtered while the right is band-pass filtered.	36
4.9	Dispersion isosurface of the synthetic wavefront with a downstream filter in place (left) and unfiltered (right).	38
4.10	Dispersion isosurface of the synthetic wavefront with a low-pass velocity-filter in place (left) and unfiltered (right).	40
4.11	Velocity low-pass filter used to determine the mean disturbance velocity. The maximum value corresponds with the actual value used in the creation of the synthetic wavefront.	41
4.12	Velocity low-pass filter used to determine the mean disturbance velocity of measured data presented in Figure 4.3. The velocity in the x-direction was measured to be 207 m/s and -17 m/s in the y-direction.	42

TABLES

SYMBOLS

Ap	Aperture size - Typically diameter
I	Actual on target intensity
I_0	Diffraction-limited intensity
k	Wavenumber ($k = 2\pi/\lambda$)
n	Index of refraction
OPD	Optical path difference
OPD _{RMS}	Spatial OPD root-mean-square
SR	Strehl ratio ($SR = I/I_0$)
Greek	
δ	Boundary layer thickness
$\langle \theta^2 \rangle$	Mean-squared of the fluctuating deflection angle

ACKNOWLEDGMENTS

CHAPTER 1

INTRODUCTION

The best possible performance of a directed energy system whether airborne or ground based in the far-field is the diffraction-limited case. The far-field intensity of a diffraction-limited beam is represented by I_0 and defined in Equation 1.1,

$$I_0 = \left(\frac{kAp^2}{8z} \right)^2 \quad (1.1)$$

where k is the wavenumber of the beam, Ap is the aperture size, and z is the distance from the aperture to the far-field. Figure 1.1 show the far-field diffraction-limited intensity of a beam as the wavelength of the beam is varied and normalized by I_0 at $1\mu\text{m}$. As the wavelength of an outgoing beam decreases the diffraction-limited performance greatly improves proportional to λ^{-2} . This provides a strong desire to move towards shorter wavelengths to take advantage of significantly increased diffraction-limited performance.

While diffraction-limited provides the best possible performance, real systems will however have reduced performance. The ratio of actual on target intensity, $I(t)$, to diffraction-limited intensity is the Strehl ratio, SR, shown here using the large aperture approximation,

$$\text{SR}(t) = \frac{I(t)}{I_0} \approx \exp \left\{ - \left[\frac{2\pi \text{OPD}_{\text{RMS}}(t)}{\lambda} \right]^2 \right\} \quad (1.2)$$

where $\text{OPD}_{\text{RMS}}(t)$ is the spatial root-mean-square of the optical path difference across the aperture. The Airborne Laser Laboratory (ALL) which ran from the 1970s to early 1980s used a $10.6 \mu\text{m}$ laser and had an estimated Strehl ratio of 95%[11]. Figure 1.2 shows a hypothetical case of varying the source wavelength while maintaining the same optical disturbance of ALL. By changing the laser source to 1 from $10 \mu\text{m}$ nets a 100 times increase in diffraction-limited performance, the actual on target intensity drops to practically zero if using a system with the same optical disturbances present on ALL.

As future airborne directed energy systems are developed, their optical disturbances (OPD_{RMS}) will need to be greatly reduced in order to achieve desired on target performance criteria. These

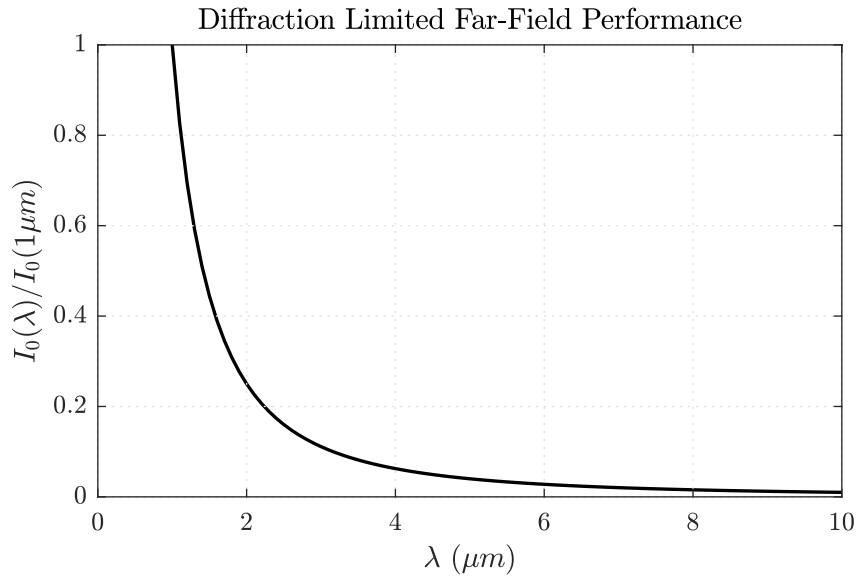


Figure 1.1. Diffraction-limited far-field intensity of a beam normalized by the performance at $1\mu m$.

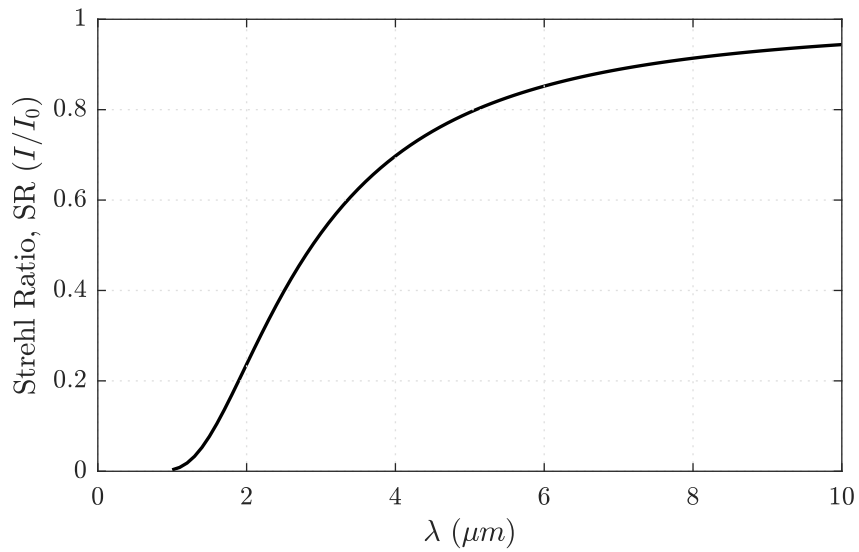


Figure 1.2. Strehl ratio due to the OPD_{RMS} of the Airborne Laser Laboratory at various laser wavelengths. ALL had an estimated Strehl ratio of 95% with its $10.6\mu m$ laser.

systems when tested on the ground in wind tunnels will see optical disturbances that are inherent to the test facility that may be on the order of the optical disturbances of the system its self. This research will look at the optical disturbance contamination that comes from the acoustic waves that travel inside of a wind tunnel.

CHAPTER 2

LITERATURE REVIEW

The literature review will consist of primarily two sections. The first section will examine aero-optics while the second will look at acoustics inside of ducts.

2.1 Aero-Optics

Optical communication and directed energy systems require a tightly focused beam on target in order to meet system performance objectives. The farfield performance of airborne optical systems can be degraded by the nearfield flow that becomes optically active at compressible flow speeds. “Aero-optics” is the study of the optical effect of these nearfield flow disturbances. Examples of important aero-optical flows that have been studied extensively include boundary layers [8, 19, 21], shear layers [5, 17], shock waves [11], and even tip vortices [16]. The effect of acoustic disturbances on aero-optical measurements has also been shown in both flight testing [4] and ground testing [2, 3].

In these optically active flows the index-of-refraction, n , varies locally as does the other fluid properties. Gladstone and Dale [6] found that the index-of-refraction is primarily a function of density with a loose dependence on the wavelength of light. Gladstone and Dale proposed a “specific refractive energy” now known as the Gladstone-Dale constant, K_{GD} ,

$$K_{GD} = \frac{n - 1}{\rho}. \quad (2.1)$$

For air the refractive index can be related to state quantities [20]

$$n - 1 = 77.6 \times 10^{-6} \frac{P}{T} \left(1 + \frac{7.53 \times 10^{-3}}{\lambda^2} \right), \quad (2.2)$$

where P is in mbar, T is in K, and λ is in μm . By combining this relationship with the ideal gas law, the Gladstone-Dale constant can be determined as a function of light wavelength,

$$K_{GD} = 2.23 \times 10^{-4} \left(1 + \frac{7.53 \times 10^{-3}}{\lambda_{\mu\text{m}}^2} \right) \left[\frac{\text{m}^3}{\text{kg}} \right]. \quad (2.3)$$

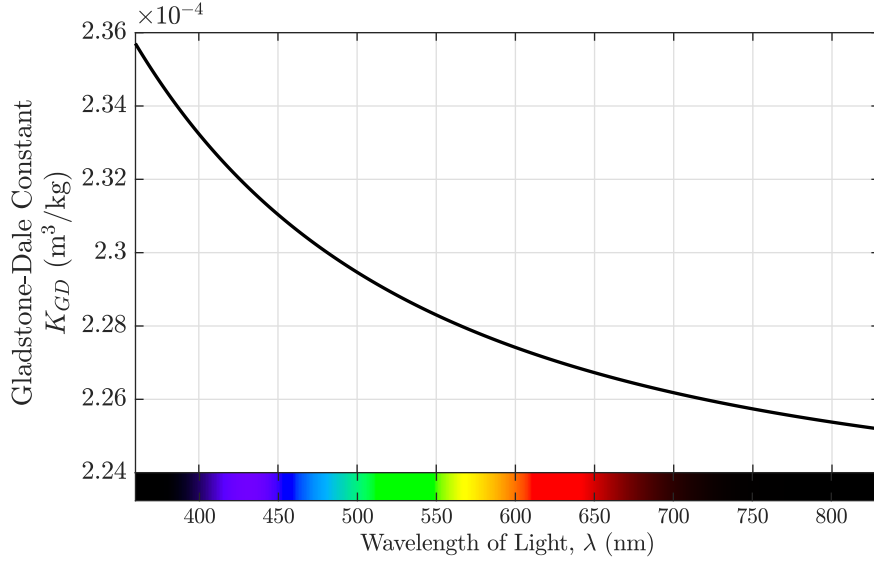


Figure 2.1. Gladstone-Dale constant for air over the visible wavelength range.

The Gladstone-Dale constant for air over the visible range is shown in Figure 2.1. While the value for K_{GD} does vary over the visible range, it is only a few percent, and many sources use an average value of $2.27 \times 10^{-4} \text{ m}^3/\text{kg}$ for the visible and near-infrared [10]. The Gladstone-Dale relationship is typically presented as

$$n = 1 + K_{GD}\rho \quad (2.4)$$

but when applied to situations where there are significant fluctuations in the flow an alternate form is often more useful

$$n' = K_{GD}\rho' \quad (2.5)$$

where $'$ denotes the quantity represents the fluctuating component ($n' = n - \bar{n}$).

When a beam with an initially planar wave front passes through a region of optical active flow its wave front aberrated. The optical path length (OPL) at any point in the beam can be obtained by integrating the index of refraction along the propagation of an optical ray [12].

$$\text{OPL}(x, y, t) = \int_{s_1}^{s_2} n(x, y, z, t) ds \quad (2.6)$$

The optical path difference (OPD), is then the spatially-averaged OPL over an aperture removed from the OPL.

$$\text{OPD}(x, y, t) = \text{OPL}(x, y, t) - \langle \text{OPL}(x, y, t) \rangle \quad (2.7)$$

When working with fluctuating components, the OPD can be calculated directly

$$\text{OPD}(x, y, t) = \int_{s_1}^{s_2} n'(x, y, z, t) ds. \quad (2.8)$$

When OPD is combined with the beam intensity profile, one can compute the farfield complex amplitude distribution using the Fraunhofer approximation [7].

$$U(x_0, y_0, t) \propto \iint_{Ap} \exp \left\{ \frac{2\pi j}{\lambda} \left[\text{OPD}(x_1, y_1, t) - \frac{(x_0 x_1 + y_0 y_1)}{z} \right] \right\} dx_1 dy_1 \quad (2.9)$$

where U is the complex amplitude, the subscripts 0 and 1 represent the coordinates of the farfield and nearfield respectively. The intensity can be computed from the complex amplitude via: $I = UU^*$. For cases in which optical aberrations are nonexistent (i.e. $\text{OPD}(x, y, t) = 0$), the farfield irradiance pattern that results from Equation 2.9 is caused entirely by diffraction from the optical aperture, and is referred to as the “diffraction-limited” irradiance pattern. For a beam with a flat wave front and circular aperture, the farfield irradiance pattern is the Airy’s disk, and the peak irradiance at the center of the disk, I_0 , is the maximum irradiance that can be achieved by the optical system:

$$I_0 = \left(\frac{kAp^2}{8z} \right)^2 \quad (2.10)$$

where k is the wavenumber ($k = 2\pi/\lambda$), Ap is the aperture diameter, and z is the distance from the aperture. In the presence of aero-optical aberrations, $\text{OPD}(x, y, t)$ is non-zero, and the farfield irradiance pattern in this case tends to be more spread out and diffuse than the diffraction-limited case; furthermore, the beam may be shifted off target by optical tip/tilt imposed by the aberrations.

The Strehl ratio (SR), is the ratio of intensity on target (I) to the diffraction-limited on target intensity (I_0):

$$\text{SR} = \frac{I}{I_0} \quad (2.11)$$

The Strehl ratio can be computed accurately by applying Equation 2.9 twice, once for the diffraction-limited case to obtain I_0 , and a second time with the OPD field due to aero-optical aberrations included to obtain I . The farfield performance, can also be estimated via the Maréchal approximation:

$$\text{SR}(t) \equiv \frac{I(t)}{I_0} \approx \exp \left\{ - \left[\frac{2\pi \text{OPD}_{\text{RMS}}(t)}{\lambda} \right]^2 \right\} \quad (2.12)$$

where OPD_{RMS} is the spatial rms of the wave front and λ is the wavelength of the beam. Equation

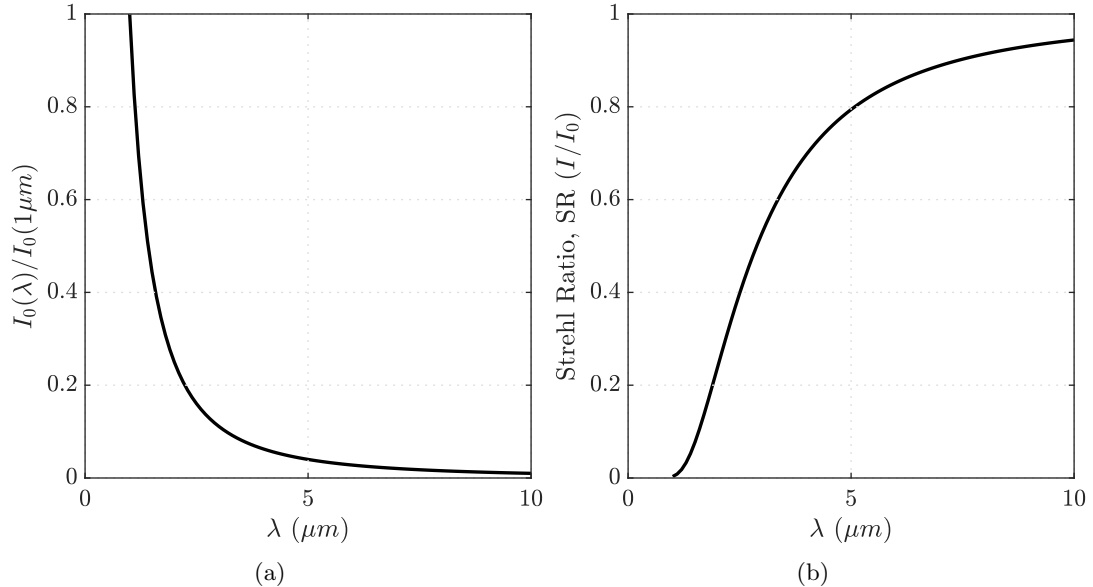


Figure 2.2. (a) Diffraction limited on target intensity as a function of wavelength normalized by the value at $\lambda = 1\mu m$. (b) Strehl ratio as a function of wavelength for an aberration that gives $SR = 0.95$ at $\lambda = 10.6\mu m$.

2.12 shows a key relationship between OPD, wavelength, and the farfield performance, plotted in Figure 2.2b. On the other hand, Equation 2.10 shows that the diffraction-limited farfield irradiance increases as the wavelength is shortened, plotted in Figure 2.2a. Together, Figure 2.2a and 2.2b show that as modern optical systems move to shorter wavelengths to increase I_0 , aero-optical aberrations cause a much more serious degradation of the Strehl ratio, illustrating why aero-optical considerations are critical in the development of any airborne optical system.

Figure 2.3 shows the OPD_{RMS} necessary to achieve various Strehl ratios over a range of wavelengths. As the wavelength of light decreases the required OPD_{RMS} decreases linearly for a fixed Strehl ratio.

2.1.1 A Brief History of Aero-Optics

The field of aero-optics began with an investigation by Liepmann [13] into the limits of sensitivity of schlieren systems when used in high-speed flow analysis. Liepmann used geometric optics to analyze a small-diameter beam and derive its mean-squared fluctuating deflection angle, $\langle\theta^2\rangle$. Liepmann propagated the beam in the y direction and assumed the index of refraction changes in the $x - z$ plane were statistically similar. Liepmann's analysis for a boundary layer of thickness δ

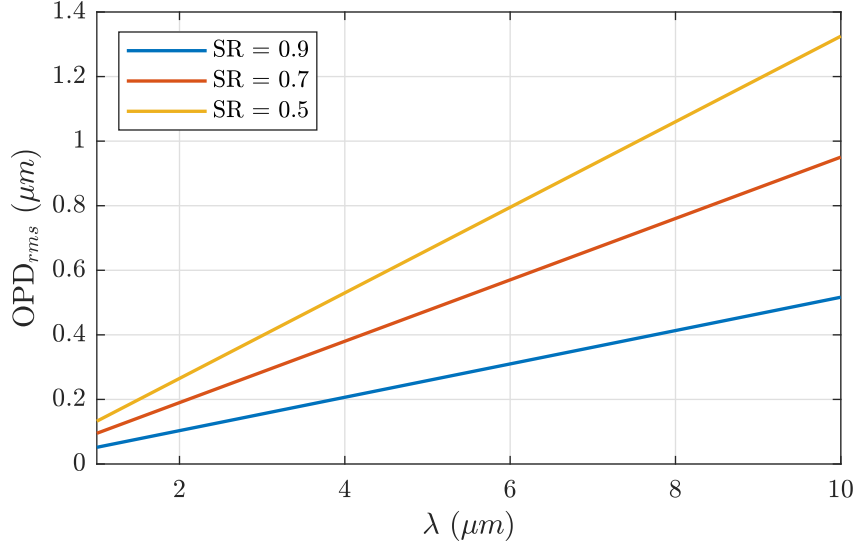


Figure 2.3. OPD_{RMS} values necessary to obtain Strehl ratios of 0.9, 0.7, and 0.5 over a range of wavelengths.

resulted in

$$\langle \theta^2 \rangle = \frac{1}{[n_0(\delta)]^2} \int_0^\delta \int_0^\delta n_0(y) n_0(\zeta) \left\langle \left(\frac{\partial \nu}{\partial y} \right)^2 \right\rangle R_v(|y - \zeta|) dy d\zeta \quad (2.13)$$

where the index of refraction is determined from $n = n_0(y)(1 + \nu)$ and $R_v(|y - \zeta|)$ is the correlation function for the index variation. This analysis introduced the concept of a linking equation that allows one to predict time-averaged optical degradation to turbulent flow statistical measurements.

2.2 Acoustics

2.2.1 Basic Acoustics

Starting with the conservation of mass,

$$\frac{\partial \rho}{\partial t} + \nabla \cdot (\rho \mathbf{u}) = 0, \quad (2.14)$$

and separating the density into a time-averaged (ρ_0) and fluctuating portion (ρ'), $\rho = \rho_0 + \rho'$. The fluctuating conservation of mass equation is obtained by separating the density ($\rho = \rho_0 + \rho'$) into a temporally averaged density, ρ_0 , and a

$$\frac{D\rho'}{Dt} + \nabla \cdot (\rho_0 \mathbf{u}) = 0 \quad (2.15)$$

For acoustics waves of frequency less than 10^9 Hz the compression of the fluid can be assumed to be adiabatic [14].

$$\left. \frac{\partial p}{\partial \rho} \right|_s = c_0^2 \quad (2.16)$$

2.2.2 Duct Acoustics

Acoustic waves are often enclosed inside of some sort of structure. This section will look at acoustics when confined to a duct in which the acoustic waves primarily travel along one-axis and have walls confining the acoustics along the other two axes as is the case inside of a wind tunnel. Figure 2.4 shows the diagram used for deriving the acoustic properties inside of a constant area duct.

This derivation is primarily influenced from Munjal [15] along with Jacobsen and Juhl [9]. The primary assumption used in this derivation is that the duct is of constant cross-section. This means that all mean quantities (ρ_0 , \mathbf{u}_0 , ...) are constant throughout space and time. Starting with the linearized inviscid forms of the conservation of mass,

$$\frac{\mathbf{D}\rho}{\mathbf{D}\mathbf{t}} + \rho_0 \nabla \cdot \mathbf{u} = 0, \quad (2.17)$$

and conservation of momentum,

$$\rho_0 \frac{\mathbf{D}\mathbf{u}}{\mathbf{D}\mathbf{t}} + \nabla p = 0. \quad (2.18)$$

The definition of the speed of sound (Equation 2.16) is then substituted into Equation 2.17,

$$\frac{1}{c_0^2} \frac{\mathbf{D}p}{\mathbf{D}\mathbf{t}} + \rho_0 \nabla \cdot \mathbf{u} = 0, \quad (2.19)$$

where c_0 is the speed of sound at average fluid properties (ρ_0 , p_0 , T_0 , ...). Next the difference between the material derivative ($\mathbf{D}/\mathbf{D}\mathbf{t}$) of Equation 2.19 and the partial derivative ($\partial/\partial\mathbf{x}$) of Equation 2.18 with respect to space is taken which results in the convected 3-D wave equation,

$$\left(\frac{\mathbf{D}^2}{\mathbf{D}\mathbf{t}^2} - c_0^2 \nabla^2 \right) p = 0. \quad (2.20)$$

Expanding the material derivative and dividing by c_0^2 ,

$$\left(\frac{1}{c_0^2} \frac{\partial^2}{\partial t^2} + \frac{2\mathbf{M}}{c_0} \frac{\partial^2}{\partial t \partial \mathbf{x}} - (1 - \mathbf{M}^2) \nabla^2 \right) p = 0, \quad (2.21)$$

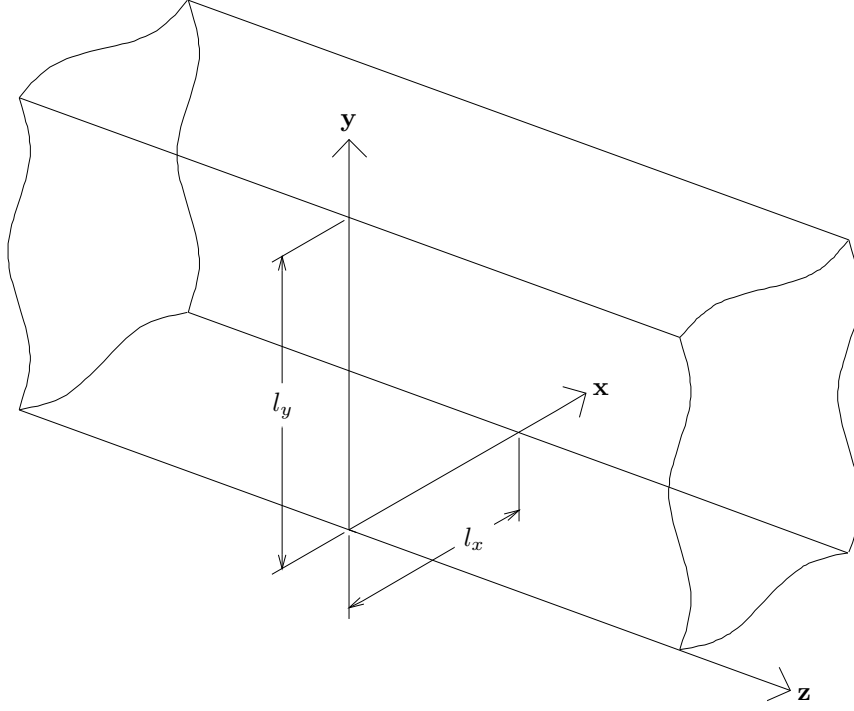


Figure 2.4. Duct with a rectangular cross-section.

where $\mathbf{M} = \mathbf{u}_0/c_0$. By using the fact that $c_0 = \omega/k_0$, Equation 2.20 can be written in a more convent form,

$$\left(\frac{1}{\omega^2} \frac{\partial^2}{\partial t^2} + \frac{2\mathbf{M}}{\omega k_0} \frac{\partial^2}{\partial t \partial \mathbf{x}} - \frac{1 - \mathbf{M}^2}{k_0^2} \nabla^2 \right) p = 0, \quad (2.22)$$

where ω is the angular frequency and k_0 is the total wavenumber.

At this point the pressure field is going to be written in a complex form and assumed to be separable in both time and space such that $\hat{p}(\mathbf{x}, t) = \hat{p}(x, y) \hat{p}(z) \hat{p}(t)$. The temporal solution is assumed to take the form

$$\hat{p}(t) = \exp \{j\omega t\}. \quad (2.23)$$

This results in the spatial component of the convecting wave equation

$$((1 - \mathbf{M}^2) \nabla^2 - 2jk_0 \mathbf{M} \nabla + k_0^2) \hat{p}(x, y) \hat{p}(z) = 0. \quad (2.24)$$

This can be further split into axial and cross-sectional components by splitting k_0 into components,

$$k_0 = \sqrt{k_{xy}^2 + k_z^2}, \quad (2.25)$$

and because the mean flow is only in the axial direction ($\mathbf{M} = M\hat{\mathbf{k}}$). The cross-sectional component is a typical Helmholtz equation

$$\left(\frac{\partial^2}{\partial x^2} + \frac{\partial^2}{\partial y^2}\right)\hat{p}_{xy}(x, y) + k_{xy}^2\hat{p}(x, y) = 0, \quad (2.26)$$

whos solution,

$$\hat{p}(x, y) = \Psi_m(x, y), \quad (2.27)$$

is one of infinity many eigen-function solutions with discrete wavenumbers, k_m . The axial component of the convecting wave equation,

$$(1 - M^2)\frac{\partial^2\hat{p}(z)}{\partial z^2} - 2jk_0M\frac{\partial\hat{p}(z)}{\partial z} + k_z^2\hat{p}(z) = 0, \quad (2.28)$$

retains the total wavenumber in second term which means its solution will depend on the cross-sectional wavenumber value at cross-sectional mode. The solution to the axial convecting wave equation,

$$\hat{p}(z) = p_m^+ \exp\{-jk_{zm}^+z\} + p_m^- \exp\{+jk_{zm}^-z\}, \quad (2.29)$$

has waves traveling in both directions with the axial wavenumber in each direction for a given mode

$$k_{zm}^\pm = \frac{\mp Mk_0 + \sqrt{k_0^2 - (1 - M^2)k_m^2}}{1 - M^2}. \quad (2.30)$$

The solution for a three-dimensional acoustic wave in a duct with a constant but arbitrary cross-section in complex pressure is the combination of the component solutions presented in Equations 2.23, 2.27, and 2.29,

$$\hat{p}(x, y, z, t) = \Psi_m(x, y) (p_m^+ \exp\{-jk_{zm}^+z\} + p_m^- \exp\{+jk_{zm}^-z\}) \exp\{j\omega t\}. \quad (2.31)$$

The two solutions for a plane wave ($\Psi_m = 1$, $k_m = 0$) traveling in a duct have a characteristic speed of $u \pm c_0$. Acoustic modes will travel indefinitely if $k_0^2 - (1 - M^2)k_m^2 > 0$ (the quantity inside of the square-root of Equation 2.30). This presents a frequency at which a given mode will cut-on,

$$f_{cuton} = \frac{c_0}{2\pi} \sqrt{(1 - M^2)k_m^2}. \quad (2.32)$$

Below this frequency, an acoustic mode will be exponentially attenuated as it travels through the

duct.

2.2.2.1 Characteristic Equations of Cross-Sections

In order to determine the characteristic equations of an acoustic field within a cross-section the solution to Equation 2.26 needs to be determined. A typical boundary condition that is used in the solution of this 2-D Helmholtz equation is using the assumption that the walls are rigid.

$$\nabla p_{x,y}(x, y) \cdot \mathbf{n}_{wall} = 0 \quad (2.33)$$

This boundary condition results in the acoustic waves being perfectly reflected off of the duct walls. There are several known empirical solution sets of the characteristic equations for specific geometry with the rigid wall assumption.

The first of these solutions is for a rectangular cross-section,

$$\Psi_{m,n}(x, y) = \cos(k_x x) \cos(k_y y), \quad (2.34)$$

where the wave numbers along each axis are $k_x = m\pi/l_x$ and $k_y = n\pi/l_y$. The duct has a width of l_x and a height of l_y . The total cross-sectional wave number for use in determining the axial wave numbers is

$$k_m^2 = k_x^2 + k_y^2. \quad (2.35)$$

Figure 2.5 shows the characteristic functions when $m=0:2$ and $n=0:3$ for a rectangular cross-section of width of l_x and height of l_y . The lines depicted in the figure are nodal lines and represent locations where there is zero pressure fluctuations for that acoustic mode.

The second set of known empirical solutions is for a circular cross-section with radius R ,

$$\Psi_{m,n}(r, \theta) = J_m(k_{mn}r) \exp\{\pm jm\theta\}, \quad (2.36)$$

where J_m is the m^{th} Bessel function of the first kind and the \pm indicates the direction of spin. If the left and right spin coefficients are equal in magnitude then a non-spinning mode is created. In order to satisfy the solid wall boundary condition $J'_m(k_{mn}R) = 0$ which determines a set of discrete values for the cross-sectional wave number at the n^{th} zero for the m^{th} Bessel function. Figure 2.6 shows the characteristic functions for a circular duct.

Characteristic Functions for a Rectangular Duct

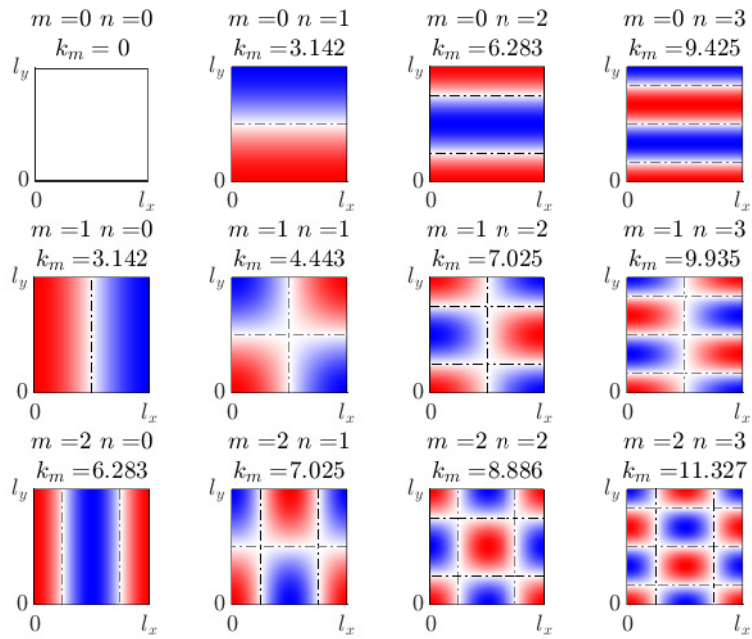


Figure 2.5. Characteristic solutions to Equation 2.26 with rigid wall in a rectangular cross-section where $m=0:2$ and $n=0:3$. Nodal lines are depicted by the dot-dash lines. The cross-sectional wave numbers, k_m , listed are for a duct of unit length and height.

Characteristic Functions for a Circular Duct

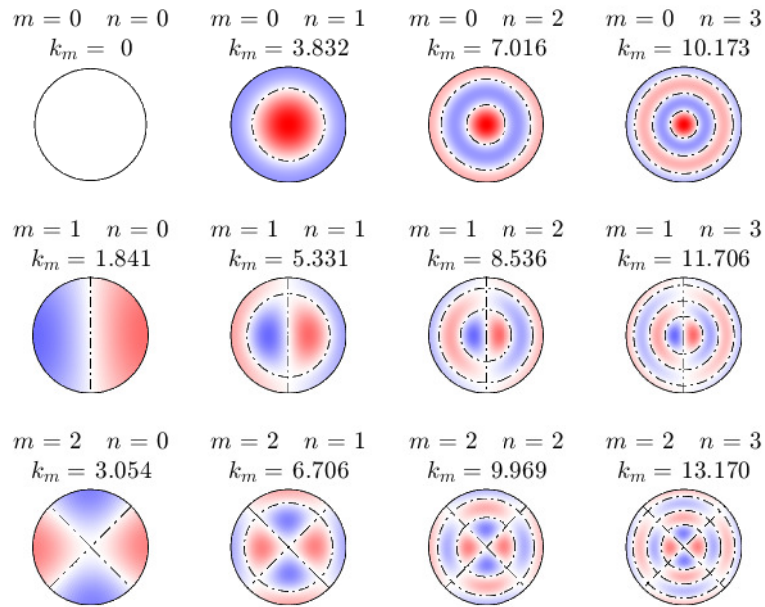


Figure 2.6. Characteristic solutions to Equation 2.26 with rigid wall in a circular cross-section where $m=0:2$ and $n=0:3$. Nodal lines are depicted by the dot-dash lines. The cross-sectional wave numbers, k_m , listed are for a duct of unit radius.

CHAPTER 3

AERO-OPTICAL AND ACOUSTICAL COUPLING

Acoustic waves are isentropic compression waves with the fluctuating pressure, p' , determining the strength of the wave. This fluctuating pressure is related to the sound pressure level, SPL by

$$\text{SPL} = 20 \log_{10} \left(\frac{p_{rms}}{p_0} \right) \quad (3.1)$$

where p_{rms} is the root mean square of the pressure fluctuation, and p_0 is the reference pressure (20 μPa for air). The pressure fluctuations can be converted to the density fluctuations via the definition of the speed of sound:

$$c_0^2 = \left(\frac{\partial p}{\partial \rho} \right)_s = \frac{p'}{\rho'} \quad (3.2)$$

where c_0 is the speed of sound at mean fluid properties and the subscript s denotes constant entropy. It can be shown by combining Equations 2.5 and 2.7 that the fluctuating density can be related to the OPD:

$$\text{OPD} = K_{GD} \int_{s_1}^{s_2} \rho' ds \quad (3.3)$$

These equations form the bases of calculating the optical effect of acoustic waves or determining the sound pressure level of a flow field from a non-intrusive optical measurement.

3.1 Examples of Acoustic-Optical Coupling

3.1.1 Planar Acoustic Waves

This section will show several plots to show the effect that acoustic waves have on the optical wavefront of a planar wave with the general geometry shown in Figure 3.1. For the following example, l_n is the width of the acoustic disturbance (for example, the width of the wind tunnel), θ is the angle between the planar acoustic wave and the beam direction, A_p is the aperture diameter of the beam, and Λ is the wavelength of the acoustic wave.

Figure 3.2 shows the time averaged OPD_{RMS} per meter of beam propagation when the beam path is parallel ($\theta = 0$) to the peaks and troughs of the planar acoustic wave as SPL is varied. As

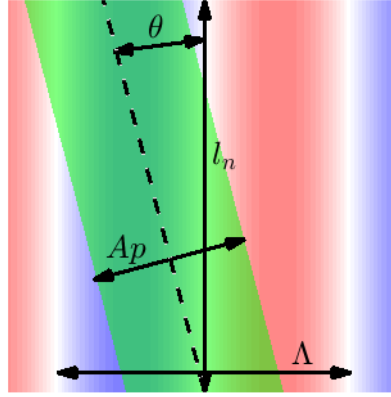


Figure 3.1. General geometry for various sample calculations for showing the acoustic-optic coupling effect.

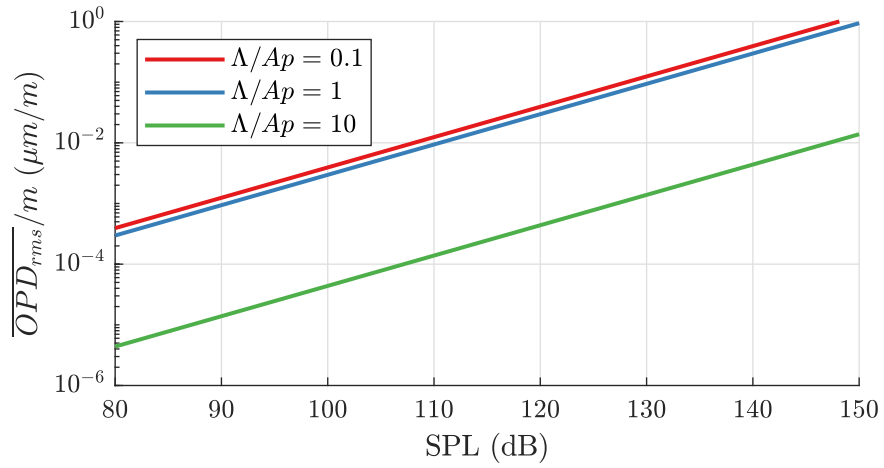


Figure 3.2. Theoretical time-averaged OPD_{RMS} per meter of beam propagation as a function of sound pressure level, SPL, for several Λ/A_p ratios and $\theta = 0$.

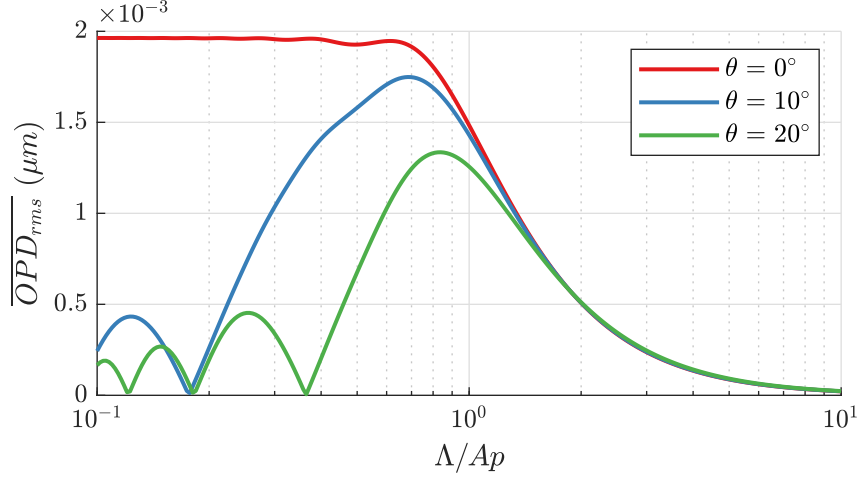


Figure 3.3. Theoretical time-averaged OPD_{RMS} for a rms sound pressure of 1 Pa (SPL of 94 dB), l_n of 1 m, and various angles and Λ/Ap ratios.

the sound pressure level increases the time averaged OPD_{RMS} also increases and can easily reach the point of being a significant factor in the measured optical disturbance. There is little difference between 0.1 and 1 Λ/Ap , but as the wavelength gets much larger compared to the beam diameter, then the optical effect of the noise is greatly reduced, this effect is known as aperture filtering [18].

Aperture filtering is more clearly shown in Figure 3.3. As the Λ/Ap ratio increases from 0.1, time-averaged OPD_{RMS} remains fairly constant until it starts to drop around Λ/Ap of 0.7 and starts to asymptotically approach zero which it basically reaches by Λ/Ap of 10. Figure 3.3 also shows the effect of changing the beam angle, θ , through the acoustic field. For nonzero θ , the beam encounters alternating high and low index of refraction as it passes through the test region, so that the time-averaged OPD_{RMS} begins to decrease compared to the $\theta = 0^\circ$ case below $\Lambda/Ap = 1$. There are also points of zero optical disturbance that occur at $\theta_{zero} = \tan^{-1}(n\Lambda/l_n)$ for $n \neq 0$; these points occur because the peaks and valleys of the optical disturbance caused by the sound wave effectively cancel out over the length of the integration path, $l_n/\cos\theta$.

Figures 3.2 and 3.3 show the optical effect of plane acoustic waves in a no-flow environment. The effect of wind-tunnel flow is to stretch (downstream-traveling waves) or compress (upstream-traveling waves) the wavelength of the acoustic noise thereby altering the filtering effect of the beam aperture. Figure 3.4 shows a typical optical disturbance from the two transverse acoustic waves (u+c and u-c) present in a wind tunnel at Mach 0.6. Both waves have a RMS sound pressure of 1 Pa and the beam has an aperture of 15 cm and propagates through a 1 m acoustic field

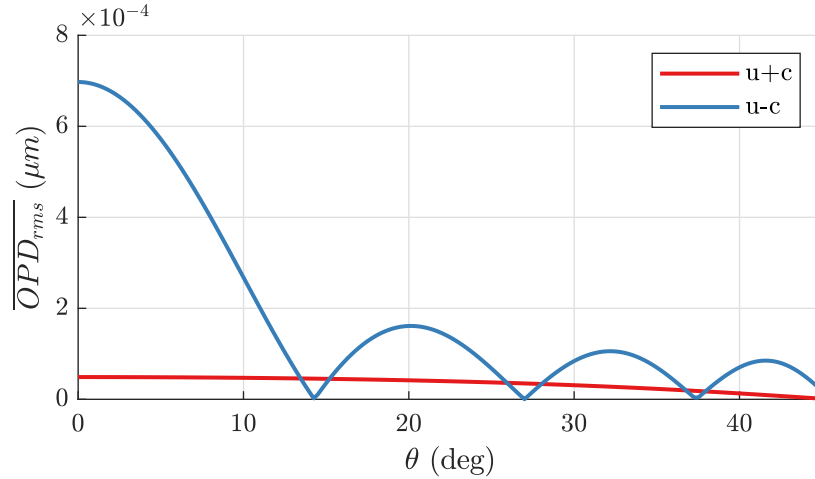


Figure 3.4. Theoretical time-averaged OPD_{RMS} for the two acoustic waves ($u+c$ and $u-c$) for the blade pass frequency (534 Hz) at Mach 0.6 with a RMS sound pressure of 1 Pa (SPL of 94 dB), l_n of 1 m, and Ap of 15 cm.

inside the tunnel. Over a vast majority of the look back angles the upstream-traveling acoustic wave has a much greater effect on the optical disturbance compared to the downstream-traveling acoustic wave, due to the much shorter wavelength of the upstream-traveling waves which is less affected by aperture filtering. However, the upstream-traveling wave goes through several zero points so the downstream-traveling wave dominates at some look back angles.

In summary, Figures 3.2 to 3.4 give an example of how planar acoustic waves are expected to affect a beam traveling a finite distance l_n at an angle θ through the acoustic field.

3.1.2 Higher Order Duct Modes

3.1.3 Spherical Acoustic Waves

CHAPTER 4

BASIC WAVEFRONT FILTERING TECHNIQUES

This chapter will examine some basic wavefront filtering techniques for removal of undesired content from an optical wavefront measurement using a synthetically generated wavefront. These basic filtering techniques are based on performing a dispersion analysis in order to compute the optical wavefronts spectral content in both time and space. These techniques are primarily designed for performing a quick analysis of measured data with some knowledge of the corruption that is present or some user intervention. It is also likely to remove some desired wavefront components and/or retain some of the measurement corruption.

4.1 Dispersion Analysis

The dispersion analysis as used in this paper is a method for calculating the power spectral density of an optical wavefront in both time and space. The result for a 2-D optical wavefront that varies over time is 3-D scalar array that lays in temporal (Hz) and spacial (m^{-1}) frequency space. Structures in the dispersion plot lay along a plane that represents its velocity in both x and y directions. A simple visualization of this is shown in Figure 4.1. This simple representation is a simulated 1-D wavefront (containing spatial data in only one dimension) that consists of two broadband planar wave structures, one that travels in the negative x -direction while the other in the positive x -direction at $5/3$ the speed. The slope of the structures are inversely related to their velocities when represented with the temporal frequency along the x -axis. The wave structure traveling in the positive x -direction has much higher frequency content, higher so than the temporal Nyquist frequency and gets aliased into the negative x -direction. Depending on the filtering methods used, this aliased information can be added no to both ends of the dispersion array in the temporal direction to artificially increase the temporal sample rate of the system. In this simplified version with the exception of the aliased data and overlap region, these two flow structures can easily be separated into two distinct wavefront components when analyzing the wavefront in frequency space.

This dispersion plot can be displayed in a different way, see Figure 4.2, such that the y -axis represents the velocity of structure if a linear trend between the spatial and temporal frequencies

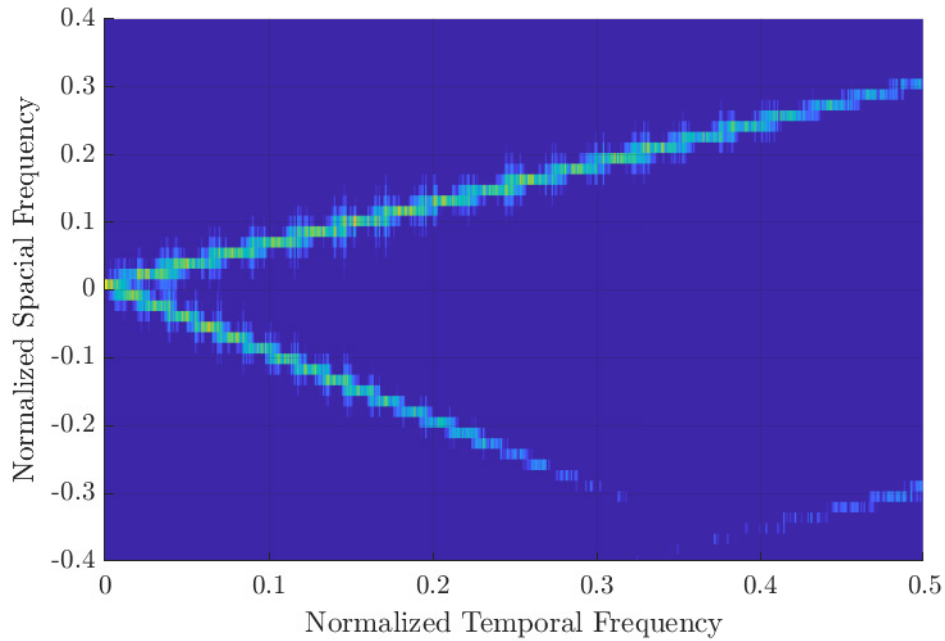


Figure 4.1. A simplified dispersion plot. Simulation of two broadband plane waves traveling in opposite directions through a 1-D wavefront.

and velocity is assumed. Here both waves that are traveling in either direction are clearly discernible, even to low frequencies and allows for the direct reading of the velocity of the group of waves. One big issue with this representation is the aliased data, which does not show up as a constant velocity as could interpret the standard dispersion plot seeing that both lines have the same slope although different y-intercept.

While these plots only show information in the x-spatial/temporal plane, the analysis can be performed in the y-spatial/temporal plane or even 3-D representations as shown in Figure 4.3. This figure shows an isosurface, which encompasses about 99.5% of the energy, of some measured data where several different prominent structures. The wing shaped structure contains the aero-optical signal of the boundary layer and free-stream turbulence. The figure-eight shaped structure is measurement noise, while the partial cone is the acoustic duct modes inside the test section. The large structure near zero-temporal frequency is a combination of vibrations and acoustic contamination, especially around the blade-pass frequency and associated harmonics.

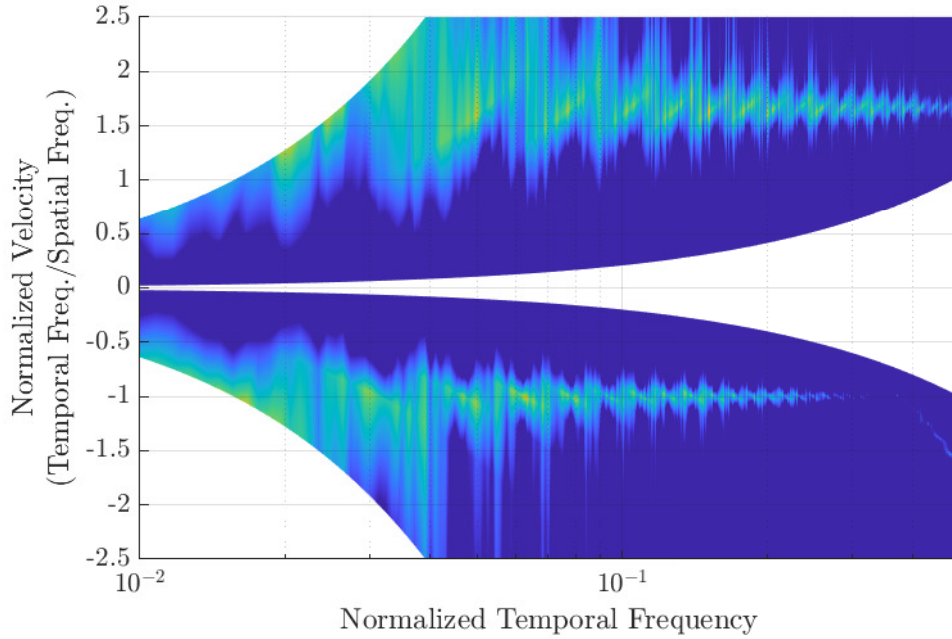


Figure 4.2. Alternative representation of the simplified dispersion plot. Simulation of two broadband plane waves traveling in opposite directions through a 1-D wavefront.

4.2 Dispersion Calculation

As the dispersion analysis is just an extension of the typical power spectra calculation,

$$S_{xx} = \frac{|\text{FFT}(x(t))|^2}{N \cdot f_{\text{samp}}}, \quad (4.1)$$

to multiple dimensions, where FFT is the Fast Fourier Transform function, N is the number of points in the transform, f_{samp} is the sample rate, and S_{xx} is the double sided power spectra. Note, that this form of the equation is for use with MATLAB's way of computing the FFT. The frequency range goes from 0 to $f_{\text{samp}} \cdot (1 - 1/N)$ in steps of f_{samp}/N and if the function `fftshift` is used on the `fft` output the range is augmented to go from $-f_{\text{samp}}/2$ to $f_{\text{samp}} \cdot (1/2 - 1/N)$ with the same frequency step size.

Because the FFT calculation assumes the signal is periodic, spectral leakage can occur when the signal is not an integer number of periods long. If minimize this spectral leakage windows are employed which typically force the end points of the signal to zero so the spectral leakage is greatly

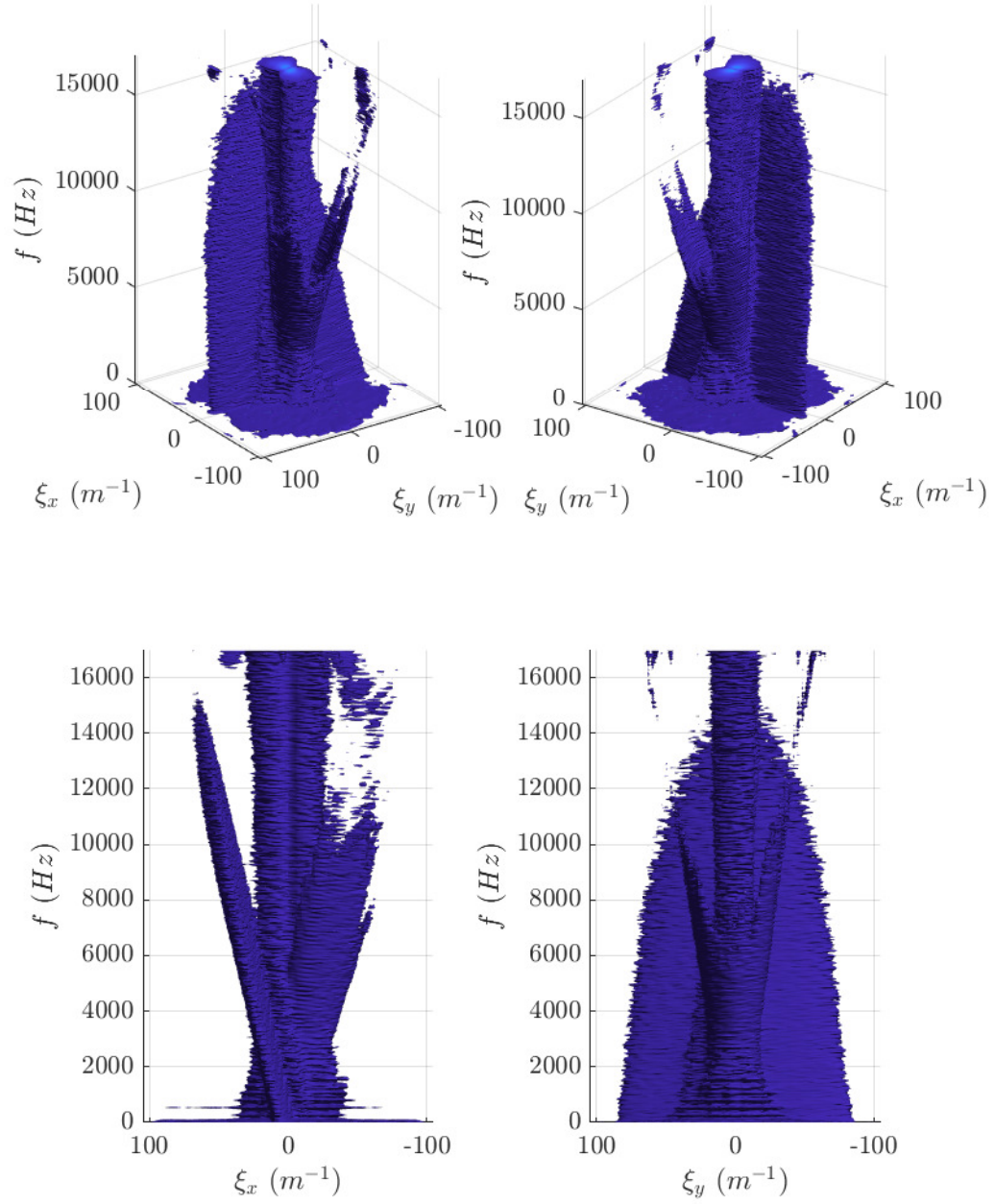


Figure 4.3. Dispersion analysis isosurface at a value of $10^{-13} \mu m^2/Hz/m^{-2}$ from two different views. The isosurface encompasses 99.5% of the energy of the optical disturbances.

reduced. The Hann window,

$$w(t) = 1/2 \left[1 - \cos \left(\frac{2\pi t}{T} \right) \right], \quad (4.2)$$

is one of the more commonly used windowing functions where $w(t)$ is the window function, t is the time at a given sample, and T is the total sample time. Since the windowing of a data set changes the signal energy some correction is needed to be applied. For an arbitrary windowing function this correction factor, c_w , is

$$c_w = \frac{1}{\sqrt{\sum w^2(t)/N}}. \quad (4.3)$$

For a Hann window this correction factor approaches $\sqrt{8/3}$ as N goes to infinity. When the equation 4.1 is combined with a windowing function and associated correction the double sided power spectra equation in one dimension becomes

$$S_{xx} = c_w \cdot \frac{|\text{FFT}\{x(t) \cdot w(t)\}|^2}{N \cdot f_{\text{samp}}}. \quad (4.4)$$

A simple MATLAB function for computing the power spectra of an one-dimension signal with an arbitrary windowing function is shown in Listing A.1.

For measurements with multiple spatial and temporal dimensions, such as typical optical wavefronts with two spatial dimensions at a discrete time interval, the Fast Fourier Transform is just applied n -times where n is the total number of dimensions, with each application in a different dimension,

$$\text{FFT}_n(x) = \text{FFT}(\text{FFT}(\cdots \text{FFT}(\text{FFT}(x, 1), 2) \cdots, n-1), n), \quad (4.5)$$

where $\text{FFT}(x, n)$ is the Fast Fourier Transform of x in the n^{th} dimension. For a n -dimensional array the power spectra the function becomes,

$$\mathbf{S}_{\mathbf{xx}} = c_w \cdot \frac{|\text{FFT}_n\{f(\mathbf{x}) \cdot w(\mathbf{x})\}|^2}{\prod \vec{N} \cdot \vec{f}_{\text{samp}}}, \quad (4.6)$$

where $\mathbf{S}_{\mathbf{xx}}$ is the n -dimensional power spectra array or dispersion array, $f(\mathbf{x})$ is a n -dimensional set of data, $w(\mathbf{x})$ is a n -dimensional windowing function, \vec{N} is a vector denoting the number of elements in each dimension, \vec{f}_{samp} is a vector denoting the sample rate in each dimension, and

$$c_w = \frac{1}{\sqrt{\sum w^2(\mathbf{x}) / \prod \vec{N}}}. \quad (4.7)$$

A simple MATLAB code for calculating the dispersion of x with an arbitrary windowing function

is shown in Listing A.2.

The optical wavefronts used throughout this paper are round apertures with no additional obscurations and is constant throughout the sample period. This allows the windowing function to be split into two separate components,

$$w(\mathbf{x}) = w_t(t) \cdot w_s(x, y), \quad (4.8)$$

the temporal windowing function, $w_t(t)$, and the spatial windowing function, $w_s(x, y)$. Both the temporal and spatial windowing functions used in this paper are Hann windows. The temporal window used the function shown in Equation 4.2, while the spatial windows used a modified version based on the normalized radius, ρ_N , of the aperture such that at the center of the aperture the weighting was one and the edge the weighting was zero and remained zero outside to the aperture,

$$w_s(\rho_N) = \begin{cases} \frac{1 + \cos(\pi \cdot \rho_N)}{2} & \text{if } \rho_N < 1 \\ 0 & \text{otherwise.} \end{cases} \quad (4.9)$$

For an arbitrary shaped aperture a windowing function can be computed by finding the minimum distance from any point within the aperture to a point outside of the aperture,

$$d_{min}(x, y) = \min \left\{ \sqrt{(x - x_O)^2 + (y - y_O)^2} \right\}, \quad (4.10)$$

where O denotes the set of points outside of the aperture. This distance is then normalized by the maximum value. The windowing function is just a slight modification of the Hann window function again,

$$w_s(x, y) = \frac{1 + \cos \{ \pi \cdot (1 - d_{min}^{norm}(x, y)) \}}{2}. \quad (4.11)$$

4.3 Synthetic Wavefront Generation

In order to best understand how some basic filters preform on a set of data, a fully known synthetic wavefront was generated such that all the various components could be generated separately with the combined product filtered and compared to the synthetic wavefront containing only relevant aero-optical data. This is done by creating an input dispersion plot where each source component is separately generated with parameters that can be modified to alter the output signal as necessary. Signals that are assumed to be statistically independent are converted into dimensional space

separately and then summed together, while signals that are assumed to be related to one another (sound and vibration components) are summed together in frequency space. Figure 4.4 shows the input dispersion plot with each signal component separately colored. The aero-optical signal is shown in red, the stationary modes in blue, duct acoustics in magenta, blade-passing frequency related corruption in green, slowly varying mean-lensing in yellow, and background in cyan.

Wavefronts were generated approximate the sample conditions in that the data presented in Figure 4.3 were measured with. The sample rate was 200 m^{-1} with $64 (2^6)$ samples in the spatial dimensions and $30,000 \text{ Hz}$ with $8192 (2^{13})$ samples in the temporal dimension. The speed of sound was chosen to be 340 m/s , with a Mach number of 0.6 , and a boundary layer velocity of 163.2 m/s ($0.8U_\infty$).

The general process of developing most of the component signals was to determine an approximate shape, normalize it in the appropriate dimensions, and scale the result by using a function derived from a hyperbola,

$$\frac{\log_{10}(WF) - b}{b^2} - \frac{\xi_{\rho_N}^2}{a^2} = 1, \quad (4.12)$$

such that the signal strength at unity of the normalized radial frequency, $\log_{10}(WF(\xi_{\rho_N} = 1))$, and the limiting slope, a/b , are inputs. This results in the signal strength of the wavefront being

$$\log_{10}(WF) = b - \sqrt{\frac{\xi_{\rho_N}^2}{m^2} + b^2}, \quad (4.13)$$

where

$$b = \frac{1}{2 \log_{10}(WF(\xi_{\rho_N} = 1))} \cdot \left(\log_{10}(WF(\xi_{\rho_N} = 1))^2 - \frac{1}{m^2} \right). \quad (4.14)$$

The code used to generate the synthetic wavefront used in this section as well as its inputs are shown in Listing A.3.

4.3.1 Aero-Optical Signal

The aero-optical signal which is approximating an optical beam passing through two boundary layers normal to the wall. This signal was approximated by creating an ellipsoid in the plane of the feature's velocity and normalizing the radius by some arbitrary factors to roughly match the shape of the measured dispersion plot shown in Figure 4.3. The dispersion magnitude was then calculated by applying Equation 4.13, with relevant code shown on Lines 19-30 of Listing A.3. In Figure 4.4 the aero-optical signal is shown in red.

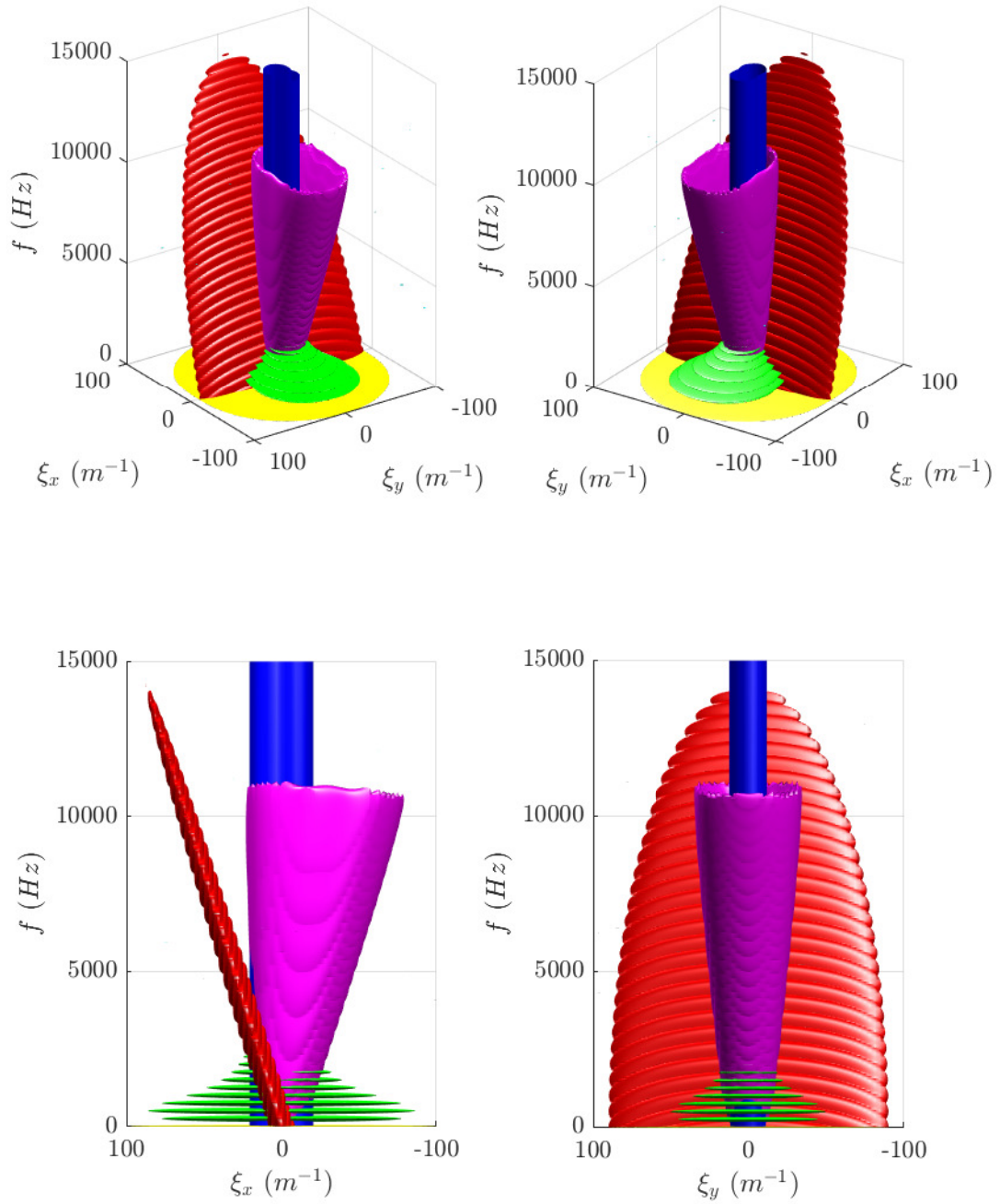


Figure 4.4. Synthetic wavefront input dispersion plot of an aero-optical signal and various signal corruption components. The aero-optical signal is shown in red, the stationary modes in blue, duct acoustics in magenta, blade-passing frequency related corruption in green, slowly varying mean-lensing in yellow, and background in cyan.

4.3.2 Stationary Mode Signals

The stationary modes in Figure 4.3 appear to be temporally white-noise with the spatial frequencies forming an epicycloid of $k = 2$. This shape was further simplified using a single trigonometric function to represent the normalization function of the radial spatial frequency,

$$\xi_{\rho_N} = \frac{\xi_{\rho}}{\xi_{\rho_0} \sqrt{10 - 6 \cos(2\xi_{\theta})}}, \quad (4.15)$$

this makes an epicycloidal like shape which has a smooth derivative. This dispersion component is shown in blue in Figure 4.4 and the relevant code shown in Lines 61-66 of Listing A.3.

4.3.3 Sound & Vibration Signals

The sound & vibrating component signals are comprised of two parts. The first of these is the blade-passing frequency and harmonic disturbances (shown in green in Figure 4.4) and the second in the acoustic duct modes (shown in magenta). Like the stationary modes, the blade-passing frequency disturbances were modeled with the simplified epicycloid narrow-band disc and each harmonic was modulated by using a low-pass filter offset to the blade-passing frequency. The code for the blade-passing frequency disturbances is shown in Lines 97-113 of Listing A.3.

The acoustic duct mode disturbances form a cone which in the $f - \xi_x$ plane is defined by the lines $u \pm c$, while in the $f - \xi_y$ plane is defined by the speed of sound. At each temporal frequency step an ellipse was defined based on the the constraining lines and the distance to that ellipse used to calculate a normalized radial frequency. The strength of the disturbance was decreased logarithmically in temporal frequency as shown in the code in Lines 183-200 of Listing A.3.

4.3.4 Mean Lensing Signal

The mean-lensing signal (shown in yellow in Figure 4.4) uses a stretched version of the simplified epicycloid and represents the slowly varying spatial disturbance. The relevant code is shown on Lines 144-152 of Listing A.3.

4.3.5 Background Noise Signal

The background noise disturbance (with a few small spots shown in cyan in Figure 4.4) was the only component that did not use the hyperbola to scale the signal but instead was just normally distributed random noise with a mean noise level and deviation as inputs. The relevant code is

shown in Lines 230-234 of Listing A.3.

4.3.6 Synthetic Wavefront Creation

A synthetic signal can be created from a power spectra by solving for x in Equation 4.1 and using the Inverse Fast Fourier Transform,

$$x(t) = \text{REAL} \left[\text{IFFT} \left\{ \sqrt{S_{xx} \cdot N \cdot f_{samp}} \cdot \exp i\phi \right\} \right], \quad (4.16)$$

where REAL is the real component and ϕ is a random set of phases for each point in the measurement space. As shown previously this relation can be extended into n -dimensions,

$$f(\mathbf{x}) = \text{REAL} \left[\text{IFFT}_n \left\{ \sqrt{\mathbf{S}_{xx} \cdot \prod \vec{N} \cdot \vec{f}_{samp}} \cdot \exp i\phi \right\} \right]. \quad (4.17)$$

Care should be taken when constructing the random set of phases, as the zero-frequency component has zero phase and the phases on either side of it are conjugates of one another. The code for creating a wavefront from a dispersion plot is shown in Lines 336-340 of Listing A.3 and is specifically creating the wavefront for the aero-optical signal but other signals are generated using the same basic code. Note that the first three lines are to get the set of phases properly configured that creates conjugate phases rotated about the origin.

It was assumed that the aero-optical signal, the stationary modes, and the background noise were statistically independent of one another and the sound & vibration combination of modes and as such could be separately transformed into physical space. While the components of the sound & vibration sources, the blade-passing frequency, the acoustic cone, and the mean-lensing, were assumed to be related to one another and thus were summed together in frequency space prior to being transformed into physical space. Once the separate components were in physical space the total wavefront was obtained by summing up the separate components with the aero-optical signal being a separately saved along side the total wavefront. Some frames from the synthetic wavefront are shown in Figure 4.5 with the total wavefront shown on top and the aero-optical only signal shown of the bottom. Flow if from right to left. The aero-optical signal is often times noticeable in the total wavefront signal but can be easily overpowered by the various contamination sources.

A dispersion plot of the total synthetic wavefront is shown in Figure 4.6. In this view the aero-optical signal is more noticeable but there still remains some significant overlap with the various contamination sources. While the mean-lensing component is not as visible in this isosurface, the

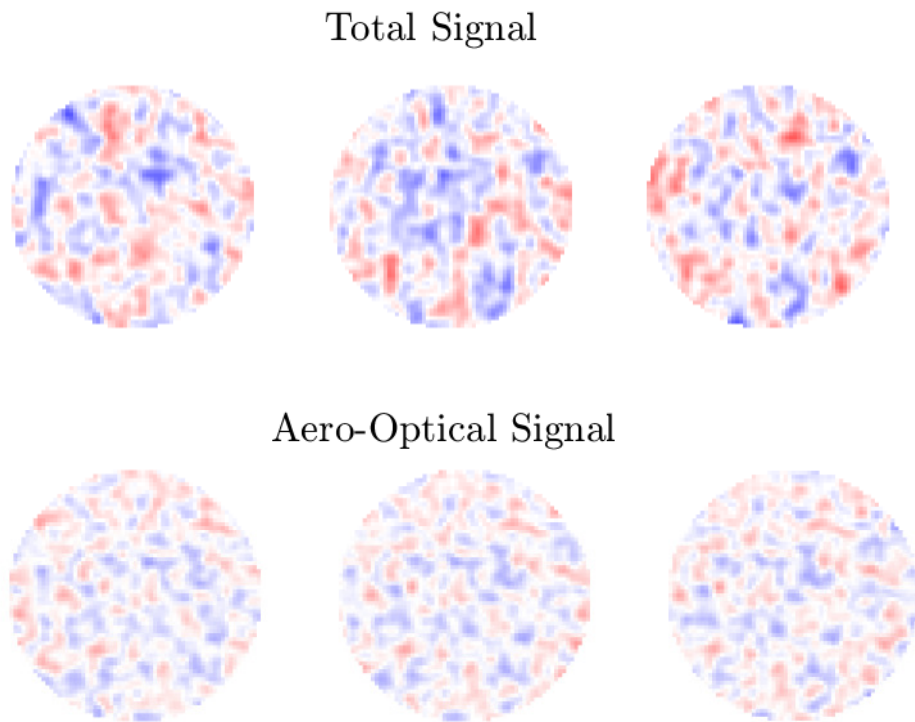


Figure 4.5. Sample frames from the synthetic wavefront with the total wavefront signal on top and the aero-optical only signal bottom. Flow is from right to left.

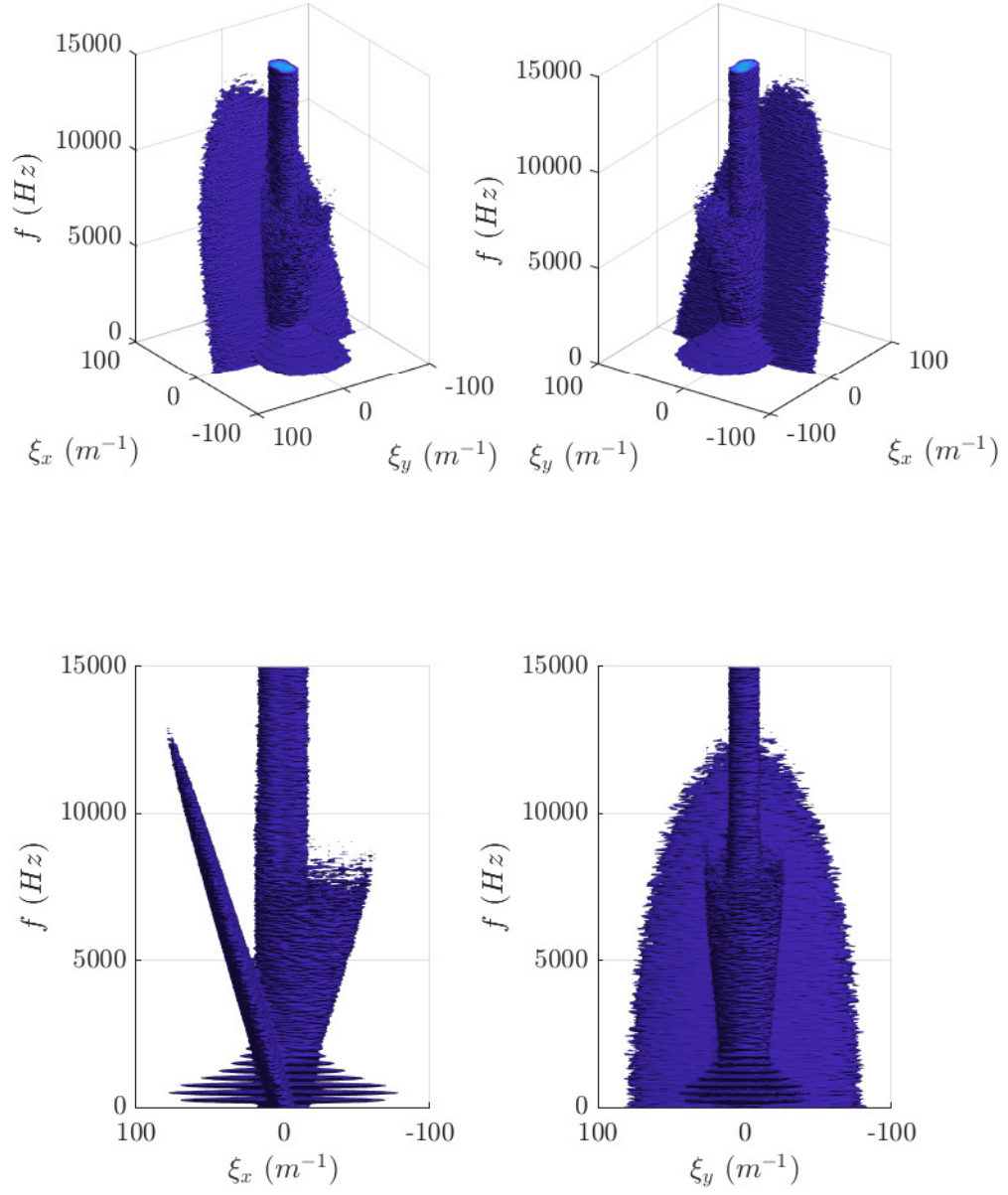


Figure 4.6. Synthetic wavefront output dispersion plot of an aero-optical signal and various signal corruption components.

rest of the dispersion plot in a good representation of the input dispersion plot shown in Figure 4.4. The total synthetic wavefront has a spatial time-averaged rms of $0.0112 \pm 0.0006\mu m$ with the aero-optical only signal having a spatial time-averaged rms of $0.0073 \pm 0.0003\mu m$. The measured wavefront presented in Figure 4.3 had a spatial time-averaged rms of $0.0874 \pm 0.0263\mu m$. The overall spatial rms of the synthetic wavefront is 12.8% when compared to the measured wavefront indicating that the algorithms used to generate the wavefront are not representative of reality and can provide a future path of research in order to produce more realistic synthetic wavefronts.

4.3.7 Comparison to Measured Data

4.4 Filtering Basics

A filter is a function, $G(\omega)$, that describes the gain a signal will experience in frequency space. In the simplest case, the filtered signal is the inverse Fourier transform of the gain multiplied by the Fourier transform of the signal. Additionally, a windowing function, $W(\mathbf{x})$, can be used to help suppress finite sampling effects,

$$f_F(\mathbf{x}) = \text{REAL} \left(\frac{\text{IFFT}_n[G(\omega) \cdot \text{FFT}_n\{f(\mathbf{x}) \cdot W(\mathbf{x})\}]}{W(\mathbf{x})} \right), \quad (4.18)$$

where f is the signal function and f_F is the filtered signal. Depending on the windowing function some data could be destroyed during this process if there is a zero present due to a divide by zero.

A basic MATLAB code for applying a filter to a wavefront using a separate function for both generating and applying the gain function which is presented in Listing A.4. This code generates a windowing function as described by Equations 4.2, 4.8, and 4.9. The temporal windowing function was generated with an additional two term such that the end point which are equal to zero could be removed to prevent the first and last frames from being destroyed due to zero being divided by zero. Likewise the normalized radius was only allow to approach one in order to prevent the lose of any sub-apertures. The filter presented in this code sample is a second order temporal high-pass filter with a cut-off frequency of 2000 Hz. The function `WFilter` takes input based on a normalized cut-point in reference to the sample rate.

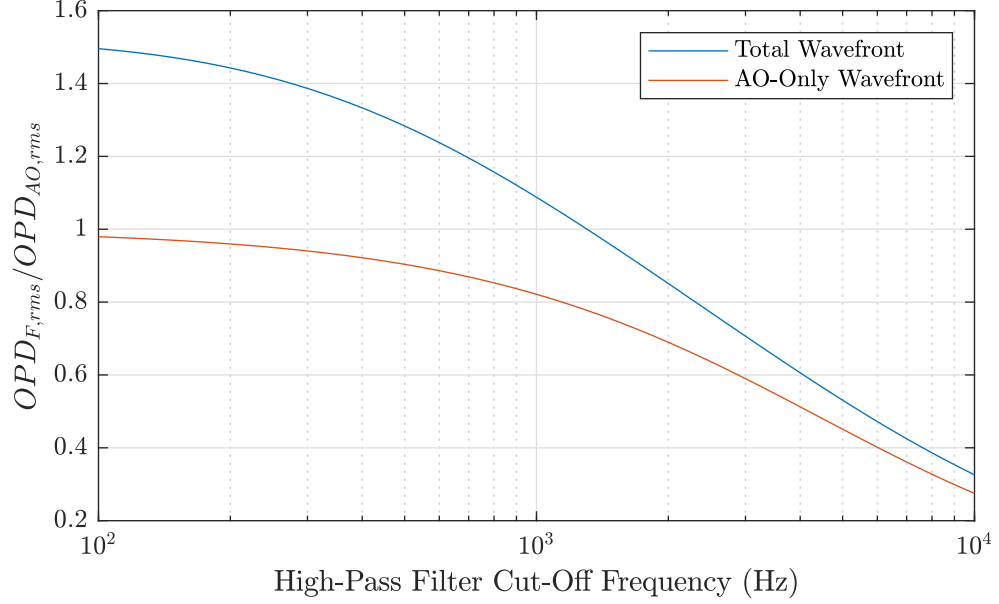


Figure 4.7. OPD time-averaged spatial-RMS of high-pass temporal filters relative to the aero-optical only unfiltered wavefront.

4.5 Temporal Filter Methods

The methods presented in this section are based on Butterworth filters [1] but could easily be extended to other types of filters. The basic gain function,

$$G(f) = \frac{1}{\sqrt{1 + \left(\frac{f}{f_c}\right)^{\pm 2n}}}, \quad (4.19)$$

where f_c is the cut-off frequency, n is the filter order (number of filters in a series), and \pm represents either a low-pass (+) or high-pass (−) filter. In this particular formulation, only the magnitude is attenuated, circuit based Butterworth filters or their digital copies will have some variable phase attenuation as well. Additionally, a band-pass filter can be constructed by placing a low-pass in series with a high-pass filter and a band-stop by placing the two types in parallel.

As a large portion of the wavefront contamination is at low frequencies, a high-pass filter is the most useful in temporal space for removing unwanted contamination, as shown in Figure 4.7. This figure shows the time-averaged spatial-RMS of both the total and aero-optical only wavefronts with various cut-off high-pass filters relative to that of the aero-optical only wavefront unfiltered. The main thing to note is that the total wavefront ratio crosses unity between around 1200 Hz, which

is about halfway between the second and third harmonic of the blade-passing frequency in this simulated wavefront. While only 75% of the aero-optical signal remains, that difference is made up by the remaining contamination signal. This can provide a very computationally cheap way estimating the aero-optical portion of the wavefront for calculations that rely on the spatial-RMS of a wavefront. While it is easy to determine a cut-off frequency for this synthetic wavefront, a measured wavefront will likely take some knowledge or expectation of the contamination that is present in the measurement.

An example of band-pass and band-stop filtering is shown in Figure 4.8. The figure shows measured data that is band-stop filtered in the left column and band-pass filtered in the right column in several different frames. The flow is from right-to-left and the band-pass filtered wavefront clearly shows upstream-moving optical disturbances associated with acoustic duct modes traveling upstream from the fan. The band-stop shows a much slower moving optical disturbance that is in general moving in the direction of the flow but it still possesses the blade-pass frequency harmonics caused optical disturbances.

One thing of note, MATLAB's builtin filter functions only work in one-dimension of frequency space so are unable to determine the direction that a signal is traveling. They also only apply the filter to the positive frequencies and zero-out the negative ones which both halves the signal passing through the filter it also switches all disturbances to moving in the same direction. So even for a filter that operates in one-dimension, it is best to apply the filter over both positive and negative frequencies to the n-dimensional Fourier transform in order to preserve the direction of travel of a signal. This Additionally allows several filters to be applied in series with one another without having to perform a Fourier and inverse Fourier transform for each successive filter.

Some additional uses of temporal filters would be in sizing and/or designing an adaptive optics system. A low-pass filter with a cut-off at the bandwidth of either a fast-steering or deformable mirror would help determine the signal that a system would need to reject. A control system may need to have the bandwidth reduced in order to keep a mirror's travel within limits. While a high-pass filter would inform designers the remaining optical aberrations that cannot be corrected and have to be lived with.

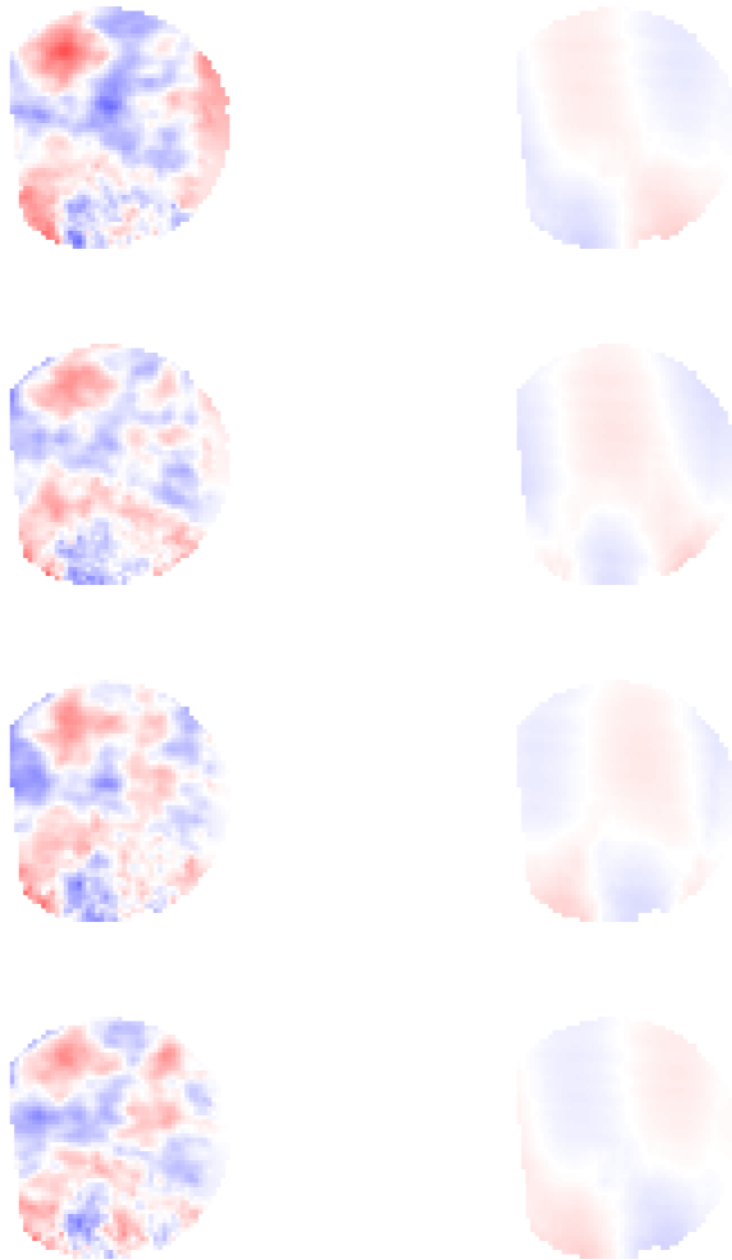


Figure 4.8. Measured wavefronts filtered at the blade-passing frequency (532 ± 10 Hz).
The left column is band-stop filtered while the right is band-pass filtered.

4.6 Upstream/Downstream Moving

For the filtering of upstream and downstream moving optical disturbances a logistic function was chosen,

$$f(x) = \frac{1}{1 + \exp\{-kx\}}. \quad (4.20)$$

This function needs to be expanded into two-dimensions (x and t) with the filter ideally returning a value of one in both the first and third quadrants and zero otherwise when wanting to obtain the disturbances moving in the direction of flow. To accomplish this the logistic curve in each dimension is scaled and offset to output values between negative one and positive one,

$$G_t(f) = \frac{2}{1 + \exp\{-k_t f\}} - 1 \quad (4.21)$$

and

$$G_x(\xi_x) = \frac{2}{1 + \exp\{\pm k_x \xi_x\}} - 1, \quad (4.22)$$

where \pm determines whether the filter is obtaining upstream traveling disturbances (+) or downstream traveling (-). These two gain functions are then multiplied together and scaled to output values between zero and one,

$$G(\xi_x, f) = \frac{(G_t \cdot G_x) + 1}{2}. \quad (4.23)$$

As the values of k_x and k_t go to infinity an ideal case is obtained where for downstream traveling disturbances have a gain of one in the first and third quadrants, zero in the second and forth quadrants, and a value of 1/2 when either frequency is zero.

The dispersion analysis using an ideal downstream moving filter on the synthetic wavefront is shown in Figure 4.9 along side the dispersion of the unfiltered wavefront. All of the upstream traveling disturbances are removed and the disturbances at $\xi_x = 0 \text{ m}^{-1}$ are significantly reduced. Some of the stationary modes remain while only the acoustic and vibration signals that are propagating in the direction of flow remain. The aero-optical signal is clipped slightly at $\xi_x = 0$ due to the spatial width of the signal. The ratio of the time-averaged spatial-RMS of the filtered signal when compared to the aero-optic only signal was 1.24 while the unfiltered ratio was 1.53. When the filter was applied to only the aero-optic signal the ratio was 0.96. This filter method is will retain any disturbance that is traveling of flow such that any contamination moving in this direction will be retained. Even with an ideal filter there is some slight attenuation of the aero-optical signal due to signal having some spectral width that crosses into upstream-moving portion of the dispersion

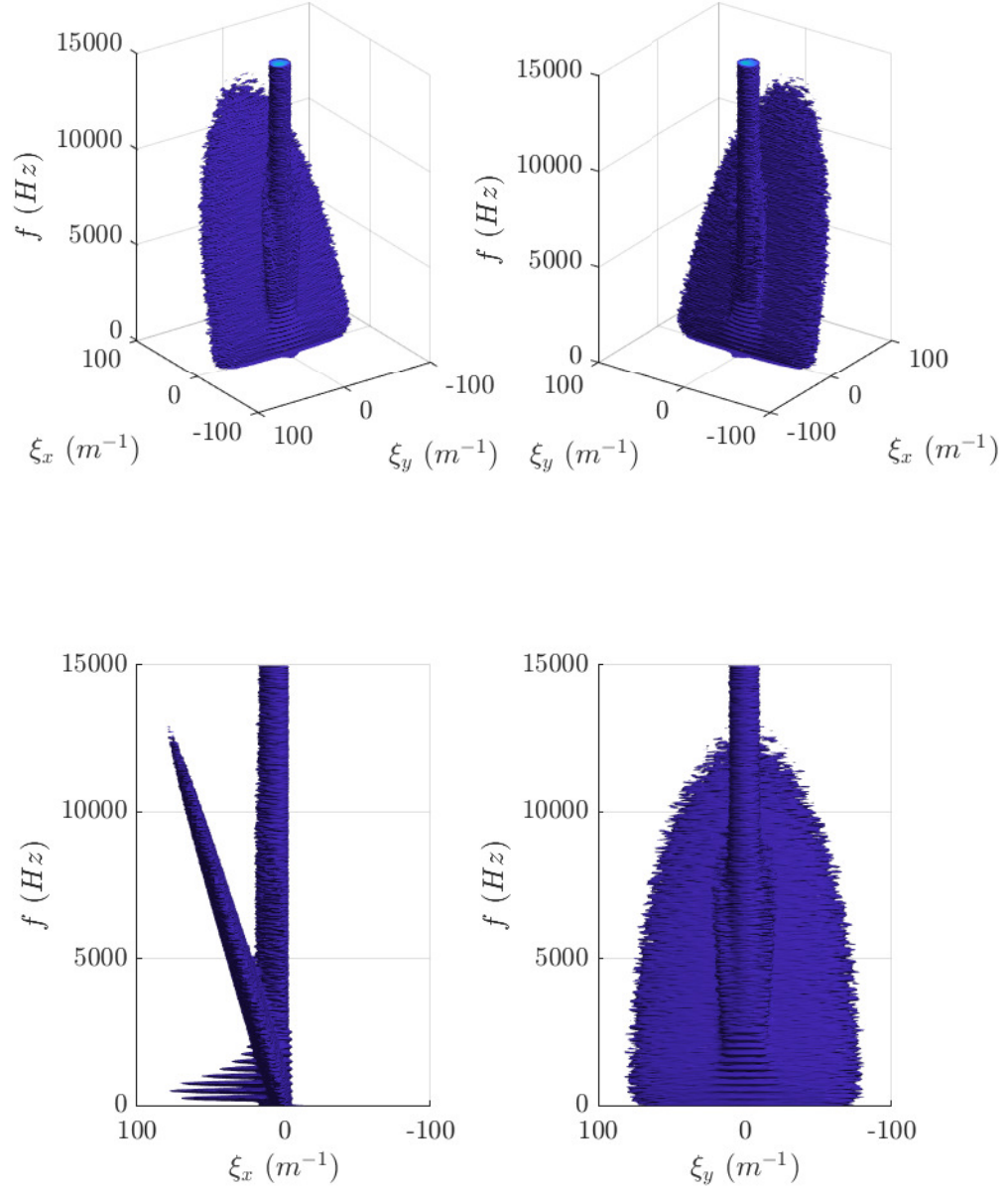


Figure 4.9. Dispersion isosurface of the synthetic wavefront with a downstream filter in place (left) and unfiltered (right).

plot.

4.7 Velocity Filtering

The dispersion plot shows flow structures that are traveling at a given speed as having a constant slope in a given direction over a large frequency range. A plane in the dispersion plot can be used to measure a flow structures velocity in both x and y -directions. The distance from any given point in the dispersion plot to a plane described by the velocities v_x and v_y

$$d = \frac{|v_x \xi_x + v_y \xi_y - f|}{\sqrt{v_x^2 + v_y^2 + 1}}. \quad (4.24)$$

A low-pass or high-pass filter can then be used to retain only disturbances that are traveling at that velocity or to exclude those disturbances respectively.

A low-pass velocity-filter of the synthetic wavefront is shown Figure 4.10. The filtered dispersion plot (left) shows primarily only the aero-optic signal remains with some additional low-frequency content from the blade-passing frequency and harmonic disturbances as well as some stationary and acoustic disturbances. The ratio of the time-averaged spatial-RMS relative to that of the aero-optical only signal went from 1.53 in the unfiltered case to 1.01 in the filtered case. This method can provide a very effective way in quickly estimating the clean spatial-RMS of a contaminated wavefront.

Another use of the synthetic wavefront is measuring the speed of a broadband disturbance such as the aero-optical signal of a boundary layer. This is done by finding the velocity that maximizes the output spatial-RMS of the velocity filter, see Figure 4.11. In this case boundary layer speed was determined to be 163 m/s which corresponds to the design velocity of the synthetic signal of $0.8U$. If the velocity range used is too large, a false result can be obtained due to the inclusion of disturbance structures not related to the aero-optical signal. For signals that have a mean-velocity component that is not aligned with an axis both velocity components can be varied as shown in Figure 4.12. In this case a variable low-pass velocity filter was employed with a high-pass spatial filter operating in the radial direction. This helped eliminate some of the low-frequency stationary disturbances as well as some of the disturbances related to the blade-passing frequency. The velocity was measured using the optical disturbances in the dispersion plot to be approximately 207 m/s in the x -direction and -17 m/s in the y -direction.

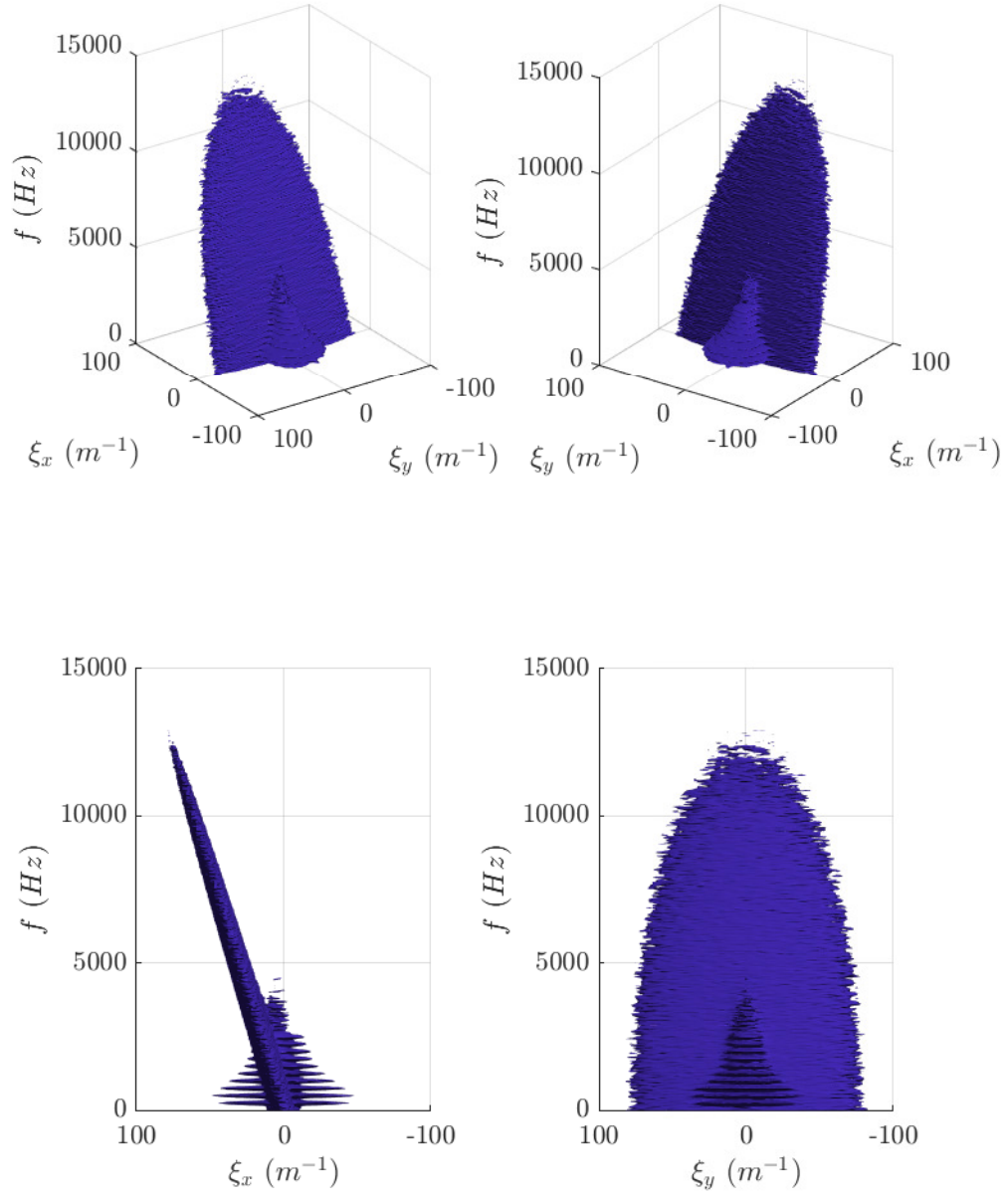


Figure 4.10. Dispersion isosurface of the synthetic wavefront with a low-pass velocity-filter in place (left) and unfiltered (right).

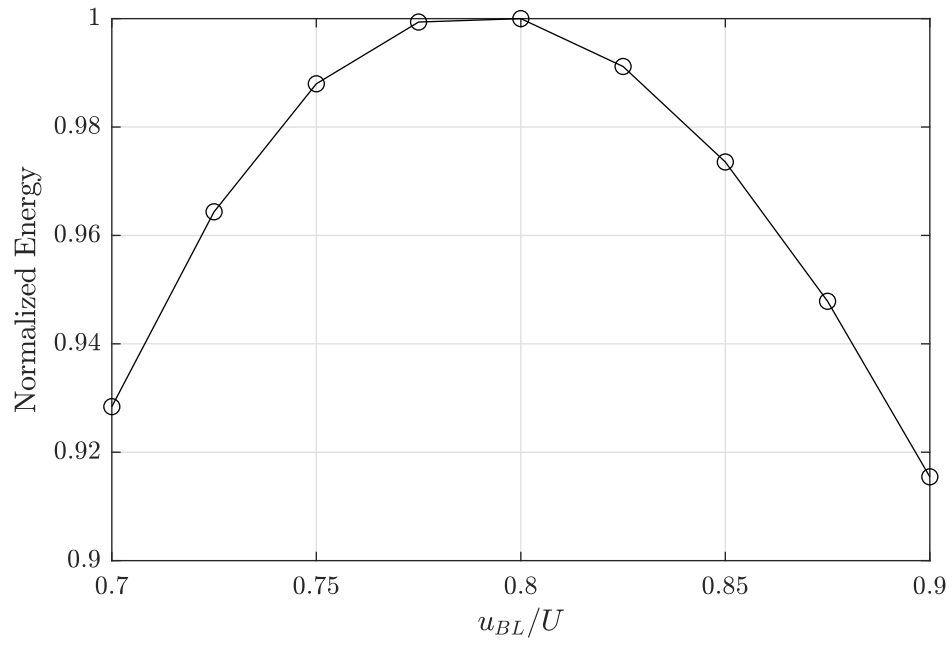


Figure 4.11. Velocity low-pass filter used to determine the mean disturbance velocity. The maximum value corresponds with the actual value used in the creation of the synthetic wavefront.

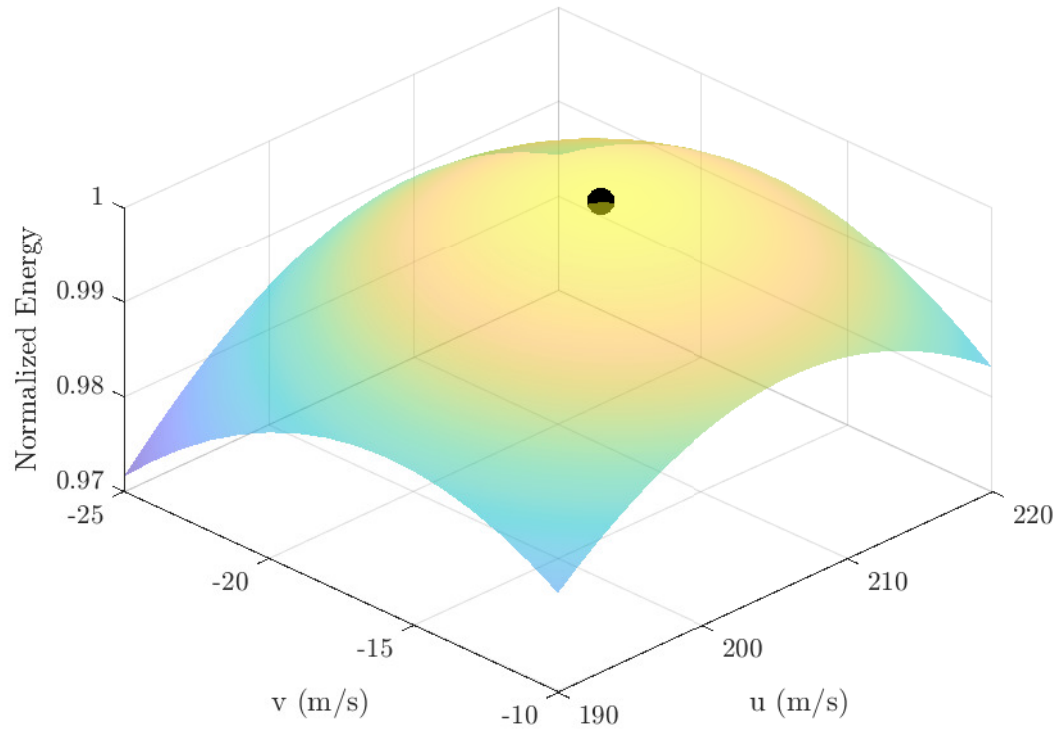


Figure 4.12. Velocity low-pass filter used to determine the mean disturbance velocity of measured data presented in Figure 4.3. The velocity in the x-direction was measured to be 207 m/s and -17 m/s in the y-direction.

APPENDIX A

SAMPLE CODE

Listing A.1: A simple function for computing the power spectra for vector x given an arbitrary windowing function.

```

1 function [sxx,freq] = simpleSXX(x,fsamp>window)
2 N = length(x);
3 x = reshape(x,1,N);
4 switch nargin
5     case 1
6         window = reshape(hann(N),1,N);
7         fsamp = 1;
8     case 2
9         window = reshape(hann(N),1,N);
10 end
11 if isempty(fsamp)
12     fsamp = 1;
13 end
14 if isa(window,'function_handle')
15     window = reshape(window(N),1,N);
16 end
17 cw = 1/sqrt(sum(window.^2,'all')/N);
18 sxx = cw*fftshift((abs(fft(x.*window))).^2)/N/fsamp;
19 freq = (-0.5:1/N:0.5-1/N)*fsamp;
20 end

```

Listing A.2: A simple function for computing the dispersion or n-dimensional power spectra of x given an arbitrary windowing function.

```

1 function [sxx,freq] = simpleSXXn(x,fsamp>window)
2 switch nargin
3     case 1
4         window = 1;
5         fsamp = ones(1,ndims(x));
6     case 2

```

```

7         window = 1;
8     end
9     if isempty(fsamp)
10         fsamp = ones(1,ndims(x));
11     end
12     cw = 1/sqrt(sum(window.^2,'all')/numel(x));
13     sxx = cw*fftshift((abs(fft(x.*window))).^2)/numel(x)/prod(fsamp);
14     for aa=1:ndims(x)
15         freq{aa} = (-0.5:1/size(x,aa):0.5-1/size(x,aa))*fsamp(aa);
16     end
17 end

```

Listing A.3: MATLAB code used to generate the synthetic wavefront used in Chapter 4.

```

1  close all; clc; clearvars; %#ok<*UNRCH
2
3  sampleRate = [200*[1 1] 30000];
4  nSamples = 2.^[6 6 13];
5  c = 340;
6  M = 0.6;
7  uBL_u = 0.8;
8  surfaceStrength = -14.5;
9  nMakePlots = 0;      % 0: off, 1: plot, 2: plot and save, 3: Combo Only
10
11 % Frequency Space
12 freq.x = (-0.5:1/nSamples(2):0.5-1/nSamples(2))*sampleRate(2);
13 freq.y = reshape((-0.5:1/nSamples(1):0.5-1/nSamples(1))*sampleRate(1),nSamples(1),1,1);
14 freq.t = reshape((-0.5:1/nSamples(3):0.5-1/nSamples(3))*sampleRate(3),1,1,nSamples(3));
15 freq.rho = sqrt(freq.x.^2+freq.y.^2);
16 freq.theta = atan2(freq.y,freq.x);
17
18 %%%% Aero-Optics Signal
19 AO.ellipsoid = [8 90 175];
20 AO.strength = -14.5;
21 AO.slope = -0.13;
22 % Calculations
23 AO.speed = c*M*uBL_u;
24 b = 1/2/AO.strength*(AO.strength^2-1/AO.slope^2);
25 AO.WF = zeros(nSamples);

```

```

26 XR = freq.x*cos(atan(-1/AO.speed))+freq.t*sin(atan(-1/AO.speed));
27 YR = freq.y;
28 TR = -freq.t*sin(atan(-1/AO.speed))+freq.x*cos(atan(-1/AO.speed));
29 R = sqrt((XR/AO.ellipsoid(1)).^2+(YR/AO.ellipsoid(2)).^2+(TR/AO.ellipsoid(3)).^2);
30 AO.WF = 10.^(b-sqrt(R.^2/AO.slope^2+b^2));
31 clear b XR YR TR R;
32
33 %%%% White-Noise Stationary Signal
34 SN.rho0 = 5;
35 SN.strength = -14.5;
36 SN.slope = -0.175;
37 % Calculations
38 b = 1/2/SN.strength*(SN.strength^2-1/SN.slope^2);
39 SN.WF = 10.^(b-sqrt(repmat((freq.rho./((SN.rho0.*sqrt(10-6*cos(2*freq.theta+pi))))
    .^2,1,1,nSamples(3))/SN.slope^2+b^2));
40 clear b;
41
42 %%%% Blade Pass Frequency Contamination
43 BPF.freq = 500;
44 BPF.harmonic = 0.5:0.5:5;
45 BPF.rho0 = 20;
46 BPF.tThickness = 100;
47 BPF.strength = -14;
48 BPF.slope = -0.13;
49 BPF.cutoff = 500;
50 BPF.aspectRatio = 1;
51 % Calculations
52 b = 1/2/BPF.strength*(BPF.strength^2-1/BPF.slope^2);
53 BPF.WF = zeros(nSamples);
54 for aa=1:length(BPF.harmonic)
55     R = sqrt((sqrt(freq.x.^2+(BPF.aspectRatio*freq.y).^2)./(BPF.rho0/sqrt(1+((BPF.
        freq*BPF.harmonic(aa)-BPF.freq)/BPF.cutoff).^2)*sqrt(10-6*cos(2*freq.theta+
        pi))))).^2+((freq.t-BPF.freq*BPF.harmonic(aa))/BPF.tThickness).^2);
56     BPF.WF = BPF.WF+10.^(b-sqrt(R.^2/BPF.slope^2+b^2));
57     R = sqrt((sqrt(freq.x.^2+(BPF.aspectRatio*freq.y).^2)./(BPF.rho0/sqrt(1+((BPF.
        freq*BPF.harmonic(aa)-BPF.freq)/BPF.cutoff).^2)*sqrt(10-6*cos(2*freq.theta+
        pi))))).^2+((freq.t+BPF.freq*BPF.harmonic(aa))/BPF.tThickness).^2);
58     BPF.WF = BPF.WF+10.^(b-sqrt(R.^2/BPF.slope^2+b^2));
59 end
60 clear b R;
61

```

```

62 Zero Frequency Contamination
63 ZERO.rho0 = 25;
64 ZERO.tThickness = 50;
65 ZERO.strength = -14.5;
66 ZERO.slope = -0.5;
67 ZERO.aspectRatio = 0.55;
68 % Calculations
69 b = 1/2/ZERO.strength*(ZERO.strength^2-1/ZERO.slope^2);
70 R = sqrt((sqrt(freq.x.^2+(ZERO.aspectRatio*freq.y).^2)./(ZERO.rho0*sqrt(10-6*cos(2*
    freq.theta+pi))))).^2+(freq.t/ZERO.tThickness).^2);
71 ZERO.WF = 10.^(b-sqrt(R.^2/ZERO.slope^2+b^2));
72 clear b R;
73
74 Acoustic Cone Signal
75 CONE.strength = [-13 -16];
76 CONE.slope = -0.3;
77 CONE.thickness = 8;
78 CONE.lowPassRho = 200;
79 CONE.lowPassX = 115;
80 % Calculations
81 freqMod.x0 = sin(0.5*atan(1/c/(M+1))+0.5*atan(1/c/(M-1)))*freq.t;
82 freqMod.y0 = 0;
83 freqMod.ax = sin(0.5*atan(1/c/(M+1))-0.5*atan(1/c/(M-1)))*freq.t;
84 freqMod.ay = sin(atan(1/c))*freq.t;
85 freqMod.theta = atan2(freq.y-freqMod.y0, freq.x-freqMod.x0);
86 freqMod.rho = (sqrt((freq.x-freqMod.x0).^2+(freq.y-freqMod.y0).^2)./sqrt((freqMod.ax
    .*cos(freqMod.theta)).^2+(freqMod.ay.*sin(freqMod.theta)).^2)-1).*sqrt((freqMod.
    ax.*cos(freqMod.theta)).^2+(freqMod.ay.*sin(freqMod.theta)).^2)/CONE.thickness;
87 freqMod.rho(:, :, end/2+1) = freq.rho(:, :)/CONE.thickness;
88 b1 = ((CONE.strength(2)-CONE.strength(1))/(sampleRate(3)/2)*abs(freq.t)+CONE.
    strength(1));
89 b = 1/2./b1.*(b1.^2-1/CONE.slope^2);
90 CONE.WF = 10.^(b-sqrt(freqMod.rho.^2/CONE.slope^2+b.^2));
91 CONE.WF = CONE.WF.*sqrt(1./(1+(freqMod.rho/CONE.lowPassRho).^2));
92 CONE.WF = CONE.WF.*sqrt(1./(1+(freq.x/CONE.lowPassX).^2));
93 clear freqMod b b1;
94
95 Background Noise
96 BACK.strength = -18;
97 BACK.deviation = 0.75;
98 % Calculations

```

```

99 BACK.WF = 10.^(randn(nSamples)*BACK.deviation+BACK.strength);
100 BACK.WF(2:nSamples(1),2:nSamples(2),nSamples(3)/2+2:nSamples(3)) = flip(flip(flip(
    BACK.WF(2:nSamples(1),2:nSamples(2),2:nSamples(3)/2),1),2),3);
101
102 %%%% Sound and Vibration
103 SV.WF = BPF.WF+ZERO.WF+CONE.WF;
104
105 %%%% Plot
106 views = [-125 25; -55 25; 180 0; 270 0];
107 f1 = figure(1);
108 for aa=1:4
109     subplot(2,2,aa)
110     patch(isosurface(freq.x,freq.y,freq.t,AO.WF,10^surfaceStrength),'edgecolor','
        none','facecolor','red','facelighting','gouraud');
111     patch(isosurface(freq.x,freq.y,freq.t,SN.WF,10^surfaceStrength),'edgecolor','
        none','facecolor','blue','facelighting','gouraud');
112     patch(isosurface(freq.x,freq.y,freq.t,BPF.WF,10^surfaceStrength),'edgecolor','
        none','facecolor','green','facelighting','gouraud');
113     patch(isosurface(freq.x,freq.y,freq.t,ZERO.WF,10^surfaceStrength),'edgecolor','
        none','facecolor','yellow','facelighting','gouraud');
114     patch(isosurface(freq.x,freq.y,freq.t,CONE.WF,10^surfaceStrength),'edgecolor','
        none','facecolor','magenta','facelighting','gouraud');
115     patch(isosurface(freq.x,freq.y,freq.t,BACK.WF,10^surfaceStrength),'edgecolor','
        none','facecolor','cyan','facelighting','gouraud');
116     grid on;
117     hold on;
118     daspect([1 1 sampleRate(3)/sampleRate(1)/3]);
119     xlim(sampleRate(1)/2*[-1 1]);
120     ylim(sampleRate(2)/2*[-1 1]);
121     zlim(sampleRate(3)/2*[0 1]);
122     camlight;
123     xlabel('$\xi_x \ (m^{-1})$', 'Interpreter','Latex');
124     ylabel('$\xi_y \ (m^{-1})$', 'Interpreter','Latex');
125     zlabel('$f \ (Hz)$', 'Interpreter','Latex');
126     % title('Synthetic Signal', 'Interpreter','Latex');
127     f1.Children(1).TickLabelInterpreter = 'latex';
128     view(views(aa,:));
129     camlight;
130 end
131 f1.Units = 'inches';
132 f1.Position = [1 1 6 8];

```

```

133 % Save Plot
134 saveas(f1, 'synthetic_wavefront.eps', 'epsc');
135
136 %%%% Animation
137 nFrames = 150;
138 theta = (0:nFrames-1)/(nFrames)*pi;
139 az = rad2deg(theta);
140 el = 25*sin(theta/2);
141
142 f2 = figure(2);
143 scolor = parula(2);
144 patch(isosurface(freq.x, freq.y, freq.t(end/2+1:end), AO.WF(:, :, end/2+1:end), 10^
        surfaceStrength), 'edgecolor', 'none', 'facecolor', 'red', 'facelighting', 'gouraud');
145 patch(isocaps(freq.x, freq.y, freq.t(end/2+1:end), AO.WF(:, :, end/2+1:end), 10^
        surfaceStrength, 'all'), 'edgecolor', 'none', 'facecolor', 'red', 'facelighting', '
        gouraud');
146 patch(isosurface(freq.x, freq.y, freq.t(end/2+1:end), SN.WF(:, :, end/2+1:end), 10^
        surfaceStrength), 'edgecolor', 'none', 'facecolor', 'blue', 'facelighting', 'gouraud')
        ;
147 patch(isocaps(freq.x, freq.y, freq.t(end/2+1:end), SN.WF(:, :, end/2+1:end), 10^
        surfaceStrength, 'all'), 'edgecolor', 'none', 'facecolor', 'blue', 'facelighting', '
        gouraud');
148 patch(isosurface(freq.x, freq.y, freq.t(end/2+1:end), BPF.WF(:, :, end/2+1:end), 10^
        surfaceStrength), 'edgecolor', 'none', 'facecolor', 'green', 'facelighting', 'gouraud'
        );
149 patch(isocaps(freq.x, freq.y, freq.t(end/2+1:end), BPF.WF(:, :, end/2+1:end), 10^
        surfaceStrength, 'all'), 'edgecolor', 'none', 'facecolor', 'green', 'facelighting', '
        gouraud');
150 patch(isosurface(freq.x, freq.y, freq.t(end/2+1:end), ZERO.WF(:, :, end/2+1:end), 10^
        surfaceStrength), 'edgecolor', 'none', 'facecolor', 'yellow', 'facelighting', 'gouraud
        ');
151 patch(isocaps(freq.x, freq.y, freq.t(end/2+1:end), ZERO.WF(:, :, end/2+1:end), 10^
        surfaceStrength, 'all'), 'edgecolor', 'none', 'facecolor', 'yellow', 'facelighting', '
        gouraud');
152 patch(isosurface(freq.x, freq.y, freq.t(end/2+1:end), CONE.WF(:, :, end/2+1:end), 10^
        surfaceStrength), 'edgecolor', 'none', 'facecolor', 'magenta', 'facelighting', '
        gouraud');
153 patch(isocaps(freq.x, freq.y, freq.t(end/2+1:end), CONE.WF(:, :, end/2+1:end), 10^
        surfaceStrength, 'all'), 'edgecolor', 'none', 'facecolor', 'magenta', 'facelighting', '
        gouraud');
154 patch(isosurface(freq.x, freq.y, freq.t(end/2+1:end), BACK.WF(:, :, end/2+1:end), 10^

```

```

        surfaceStrength), 'edgecolor', 'none', 'facecolor', 'cyan', 'facelighting', 'gouraud')
    ;
155 patch(isocaps(freq.x, freq.y, freq.t(end/2+1:end), BACK.WF(:, :, end/2+1:end), 10^
        surfaceStrength, 'all'), 'edgecolor', 'none', 'facecolor', 'cyan', 'facelighting', '
        gouraud');
156 grid on;
157 daspect([1 1 50]);
158 xlim(sampleRate(1)/2*[-1 1]);
159 ylim(sampleRate(2)/2*[-1 1]);
160 zlim(sampleRate(3)/2*[0 1]);
161 xlabel('$\xi_x \ (m^{-1})$', 'Interpreter', 'Latex');
162 ylabel('$\xi_y \ (m^{-1})$', 'Interpreter', 'Latex');
163 zlabel('$f \ (Hz)$', 'Interpreter', 'Latex');
164 f2.Children(1).TickLabelInterpreter = 'latex';
165 f2.Units = 'inches';
166 f2.Position = [1 1 5.5 6.25];
167 cl = camlight;
168
169 filename = 'synthetic_wavefront.gif';
170 frameRate = 15;
171 for aa=1:nFrames-1
172     view(az(aa), el(aa));
173     camlight(cl);
174     drawnow;
175     frame = getframe(f2);
176     im = frame2im(frame);
177     [imind, cm] = rgb2ind(im, 256);
178     if aa==1
179         imwrite(imind, cm, filename, 'gif', 'Loopcount', inf, 'DelayTime', 1/frameRate);
180     else
181         imwrite(imind, cm, filename, 'gif', 'WriteMode', 'append', 'DelayTime', 1/frameRate
            );
182     end
183 end
184
185 %%%% Make Wavefronts
186 [wf.x, wf.y] = meshgrid(0.975*(-1/2/(nSamples(1)-1):1), 0.975*(-1/2/(nSamples(2)-1):1)
    );
187 wf.rho = sqrt(wf.x.^2+wf.y.^2);
188 wf.theta = atan2(wf.y, wf.x);
189 wf.mask = ones(size(wf.x));

```



```

190 wf.mask(wf.rho>1) = NaN;
191 wf.x = wf.x.*wf.mask;
192 wf.y = wf.y.*wf.mask;
193 wf.rho = wf.rho.*wf.mask;
194 wf.theta = wf.theta.*wf.mask;
195 wf.sampleRate = sampleRate;
196 % Aero-Optics Signal
197 phase = pi*(2*rand(nSamples)-1);
198 phase(nSamples(1)/2+1,nSamples(2)/2+1,nSamples(3)/2+1) = 0;
199 phase(2:nSamples(1),2:nSamples(2),nSamples(3)/2+2:nSamples(3)) = -flip(flip(flip(
    phase(2:nSamples(1),2:nSamples(2),2:nSamples(3)/2),1),2),3);
200 wf.AO = real(ifftn(ifftshift(sqrt((AO.WF)*prod(sampleRate)*numel(AO.WF)).*exp(1i*
    phase))));
201 wf.AO = wf.AO.*wf.mask;
202 clear phase;
203 % White-Noise Stationary Signal
204 phase = pi*(2*rand(nSamples)-1);
205 phase(nSamples(1)/2+1,nSamples(2)/2+1,nSamples(3)/2+1) = 0;
206 phase(2:nSamples(1),2:nSamples(2),nSamples(3)/2+2:nSamples(3)) = -flip(flip(flip(
    phase(2:nSamples(1),2:nSamples(2),2:nSamples(3)/2),1),2),3);
207 wft.SN = real(ifftn(ifftshift(sqrt((SN.WF)*prod(sampleRate)*numel(SN.WF)).*exp(1i*
    phase))));
208 wft.SN = wft.SN.*wf.mask;
209 clear phase;
210 % Background Noise
211 phase = pi*(2*rand(nSamples)-1);
212 phase(nSamples(1)/2+1,nSamples(2)/2+1,nSamples(3)/2+1) = 0;
213 phase(2:nSamples(1),2:nSamples(2),nSamples(3)/2+2:nSamples(3)) = -flip(flip(flip(
    phase(2:nSamples(1),2:nSamples(2),2:nSamples(3)/2),1),2),3);
214 wft.BACK = real(ifftn(ifftshift(sqrt((BACK.WF)*prod(sampleRate)*numel(BACK.WF)).*exp
    (1i*phase))));
215 wft.BACK = wft.BACK.*wf.mask;
216 clear phase;
217 % Sound and Vibration
218 phase = pi*(2*rand(nSamples)-1);
219 phase(nSamples(1)/2+1,nSamples(2)/2+1,nSamples(3)/2+1) = 0;
220 phase(2:nSamples(1),2:nSamples(2),nSamples(3)/2+2:nSamples(3)) = -flip(flip(flip(
    phase(2:nSamples(1),2:nSamples(2),2:nSamples(3)/2),1),2),3);
221 wft.SV = real(ifftn(ifftshift(sqrt((SV.WF)*prod(sampleRate)*numel(SV.WF)).*exp(1i*
    phase))));
222 wft.SV = wft.SV.*wf.mask;

```

```

223 clear phase;
224 % Total
225 wf.wf = wf.AO+wft.SN+wft.BACK+wft.SV;
226 % Save
227 % save('synthetic_wavefront.mat', 'wf');
228 % disp('File Saved');

```

Listing A.4: MATLAB code used to filter wavefronts in Chapter 4.

```

1 function [wf] = WFilter(wf,varargin)
2 %WFFILTER Summary of this function goes here
3 % Detailed explanation goes here
4
5 % Check Number of Inputs
6 if mod(nargin,2)==0 || nargin<3
7     error('Invalid Number of Inputs');
8 end
9 % Zero-Out NaN Values
10 mask = double(~isnan(wf(:, :, 1)));
11 mask(mask==0) = NaN;
12 % disp(mask);
13 wf(isnan(wf)) = 0;
14 % 3D-FFT
15 wf = fftshift(fftn(wf));
16 % Calculate Frequency
17 BlockSize = size(wf);
18 Frequency.y = reshape(-1/2:1/BlockSize(1):1/2-1/BlockSize(1), [], 1);
19 Frequency.x = reshape(-1/2:1/BlockSize(2):1/2-1/BlockSize(2), 1, []);
20 Frequency.t = reshape(-1/2:1/BlockSize(3):1/2-1/BlockSize(3), 1, 1, []);
21 Frequency.rho = sqrt(Frequency.x.^2+Frequency.y.^2);
22 % Filters
23 for aa=1:length(varargin)/2
24     switch lower(varargin{2*aa-1})
25         case 'time-highpass'
26             if length(varargin{2*aa})==1
27                 n = 1;
28             else
29                 n = varargin{2*aa}(2);
30             end
31             [b,a] = butter(n,varargin{2*aa}(1), 'high', 's');
32             gain = abs(reshape(freqz(b,a,reshape(Frequency.t,1,[])), 1, 1, []));

```

```

33         clear b a;
34     case 'time-lowpass'
35         if length(varargin{2*aa})==1
36             n = 1;
37         else
38             n = varargin{2*aa}(2);
39         end
40         [b,a] = butter(n,varargin{2*aa}(1),'low','s');
41         gain = abs(reshape(freqs(b,a,reshape(Frequency.t,1,[])),1,1,[]));
42         clear b a;
43     case {'time-passband' 'time-bandpass'}
44         if length(varargin{2*aa})==2
45             n = 1;
46         else
47             n = varargin{2*aa}(3);
48         end
49         [b,a] = butter(n,varargin{2*aa}(1:2),'bandpass','s');
50         gain = abs(reshape(freqs(b,a,reshape(Frequency.t,1,[])),1,1,[]));
51         clear b a;
52     case {'time-bandstop' 'time-stop'}
53         if length(varargin{2*aa})==2
54             n = 1;
55         else
56             n = varargin{2*aa}(3);
57         end
58         [b,a] = butter(n,varargin{2*aa}(1:2),'stop','s');
59         gain = abs(reshape(freqs(b,a,reshape(Frequency.t,1,[])),1,1,[]));
60         clear b a;
61     case 'space-highpass'
62         if length(varargin{2*aa})==1
63             n = 1;
64         else
65             n = varargin{2*aa}(2);
66         end
67         gain = sqrt(1./(1+(Frequency.rho/varargin{2*aa}(1)).^(-2*n)));
68     case 'space-lowpass'
69         if length(varargin{2*aa})==1
70             n = 1;
71         else
72             n = varargin{2*aa}(2);
73         end

```

```

74         gain = sqrt(1./(1+(Frequency.rho/varargin{2*aa}(1)).^(+2*n)));
75     case 'velocity-highpass'
76         if length(varargin{2*aa})==3
77             n = 1;
78         else
79             n = varargin{2*aa}(4);
80         end
81         dist = abs(varargin{2*aa}(1)*Frequency.x+varargin{2*aa}(2)*Frequency.y-
82             Frequency.t)/sqrt((varargin{2*aa}(1))^2+(varargin{2*aa}(2))^2+1);
83         gain = sqrt(1./(1+(dist/varargin{2*aa}(3)).^(-2*n)));
84     case 'velocity-lowpass'
85         if length(varargin{2*aa})==3
86             n = 1;
87         else
88             n = varargin{2*aa}(4);
89         end
90         dist = abs(varargin{2*aa}(1)*Frequency.x+varargin{2*aa}(2)*Frequency.y-
91             Frequency.t)/sqrt((varargin{2*aa}(1))^2+(varargin{2*aa}(2))^2+1);
92         gain = sqrt(1./(1+(dist/varargin{2*aa}(3)).^(+2*n)));
93     case 'x-space'
94         switch length(varargin{2*aa})==1
95             case 1
96                 n = 1;
97                 threeDB = 0;
98             case 2
99                 n = varargin{2*aa}(2);
100                threeDB = 0;
101             case 3
102                 n = varargin{2*aa}(2);
103                 threeDB = varargin{2*aa}(3);
104         end
105         if isempty(n)
106             n = 1;
107         end
108         if threeDB
109             gain = 1./(1+exp(-n*(Frequency.x-varargin{2*aa}(1)-log(sqrt(2)-1)/n)
110                 ));
111         else
112             gain = 1./(1+exp(-n*(Frequency.x-varargin{2*aa}(1))));
113         end
114     case 'y-space'

```

```

112         switch length(varargin{2*aa})==1
113             case 1
114                 n = 1;
115                 threeDB = 0;
116             case 2
117                 n = varargin{2*aa}(2);
118                 threeDB = 0;
119             case 3
120                 n = varargin{2*aa}(2);
121                 threeDB = varargin{2*aa}(3);
122         end
123         if isempty(n)
124             n = 1;
125         end
126         if threeDB
127             gain = 1./(1+exp(-n*(Frequency.y-varargin{2*aa}(1)-log(sqrt(2)-1)/n)
128                 ));
129         else
130             gain = 1./(1+exp(-n*(Frequency.y-varargin{2*aa}(1)))));
131         end
132     case 'forward-moving'
133         kx = BlockSize(2);
134         kt = BlockSize(3);
135         if ~isempty(varargin{2*aa})
136             kx = kx*varargin{2*aa}(1);
137             kt = kt*varargin{2*aa}(2);
138         end
139         gain = (2./(1+exp(-kx*Frequency.x))-1).*(2./(1+exp(-kt*Frequency.t))-1)
140             /2+0.5;
141     case 'backward-moving'
142         kx = BlockSize(2);
143         kt = BlockSize(3);
144         if ~isempty(varargin{2*aa})
145             kx = kx*varargin{2*aa}(1);
146             kt = kt*varargin{2*aa}(2);
147         end
148         gain = (2./(1+exp(kx*Frequency.x))-1).*(2./(1+exp(-kt*Frequency.t))-1)
149             /2+0.5;
150     case 'forward-moving-ideal'
151         gain = sign(Frequency.x.*Frequency.t)/2+0.5;
152     case 'backward-moving-ideal'

```

```

150         gain = -sign(Frequency.x.*Frequency.t)/2+0.5;
151     case { 'unity' 'no-filter' }
152         gain = 1;
153     otherwise
154         warning('Invalid Filter Type. Setting Gain to Unity. ');
155         gain = 1;
156     end
157 %     disp(max(gain,[], 'all'));
158 %     disp(min(gain,[], 'all'));
159     wf = wf.*gain;
160     clear gain n;
161 end
162 % 3D-iFFT
163 wf = real(ifftn(ifftshift(wf))).*mask;
164 end

```


BIBLIOGRAPHY

1. S. Butterworth. On the theory of filter amplifiers. *Experimental Wireless and the Wireless Engineer*, 7:536–541, 1930.
2. B. L. Catron, M. R. Rennie, S. Gordeyev, and E. J. Jumper. Effect of acoustic disturbances on aero-optical measurements. In *2018 Plasmadynamics and Lasers Conference*, 2018. doi: 10.2514/6.2018-3903.
3. B. L. Catron, M. R. Rennie, S. Gordeyev, and E. J. Jumper. Filtering of acoustic disturbances from aero-optical measurements. In *AIAA Scitech 2020 Forum*, 2020. doi: 10.2514/6.2020-0683.
4. N. De Lucca, S. Gordeyev, E. J. Jumper, and D. J. Wittich. Effects of engine acoustic waves on optical environment around turrets in-flight on aaol-t. *Optical Engineering*, 57(6), 2018. doi: 10.1117/1.OE.57.6.064107.
5. E. J. Fitzgerald and E. J. Jumper. The optical distortion mechanism in a nearly incompressible free shear layer. *Journal of Fluid Mechanics*, 512:153–189, 2004. doi: 10.1017/S0022112004009553.
6. J. H. Gladstone and T. P. Dale. Researches on the refraction, dispersion, and sensitiveness of liquids. *Philosophical Transactions of the Royal Society of London*, 153:317–343, 1863.
7. J. W. Goodman. *Introduction to Fourier Optics*. McGraw-Hill, 1968.
8. S. Gordeyev, A. E. Smith, J. A. Cress, and E. J. Jumper. Experimental studies of aero-optical properties of subsonic turbulent boundary layers. *Journal of Fluid Mechanics*, 740:214–253, 2014. doi: 10.1017/jfm.2013.658.
9. F. Jacobsen and P. M. Iler Juhl. *Fundamentals of General Linear Acoustics*. John Wiley & Sons, 2013.
10. W. C. G. Jr., Y. Hidaka, and T. Tanzawa. Refractivity of combustion gases. *Combustion and Flame*, 40:213–219, 1980. doi: 10.1016/0010-2180(81)90124-3.
11. E. J. Jumper, M. A. Zenk, S. Gordeyev, D. Cavalieri, and M. R. Whiteley. Airborne aero-optics laboratory. *Optical Engineering*, 52(7), 2013. doi: 10.1117/1.OE.52.7.071408.
12. M. V. Klein and T. E. Furtak. *Optics*. John Wiley & Sons, 2nd edition, 1986.
13. H. W. Liepmann. Deflection and diffusion of a light ray passing through a boundary layer. Technical Report SM-14397, Douglas Aircraft Company, Santa Monica Division, May 1952.
14. P. M. Morse and K. U. Ingard. *Theoretical Acoustics*. McGraw-Hill, 1968.
15. M. L. Munjal. *Acoustics of Ducts and Mufflers*. John Wiley & Sons, 2nd edition, 2014.
16. C. Porter, M. Rennie, and E. Jumper. Aero-optic effects of a wingtip vortex. *AIAA Journal*, 51(7):1533–1541, 2013. doi: 10.2514/1.J050899.
17. R. M. Rennie, D. A. Duffin, and E. J. Jumper. Characterization and aero-optic correction of a forced two-dimensional weakly compressible shear layer. *AIAA Journal*, 46(11):2787–2795, 2008. doi: 10.2514/1.35290.

18. J. P. Siegenthaler, S. Gordeyev, and E. Jumper. Shear layers and aperture effects for aero-optics. In *36th AIAA Plasmadynamics and Lasers Conference*, 2005. doi: 10.2514/6.2005-4772.
19. A. E. Smith, S. Gordeyev, and E. J. Jumper. Recent measurements of aero-optical effects caused by subsonic boundary layers. *Optical Engineering*, 52(7), 2013. doi: 10.1117/1.OE.52.7.071404.
20. S. L. Valley. Handbook of geophysics and space environments. Technical Report ADA056800, Air Force Cambridge Research Laboratories, April 1965.
21. K. Wang and M. Wang. Aero-optics of subsonic turbulent boundary layers. *Journal of Fluid Mechanics*, 696:122–151, 2012. doi: 10.1017/jfm.2012.11.